Master Thesis

RWTH Aachen/FZ Jülich

August 3, 2020

Alexander Neukirchen

Source-Free Exchange-Correlation Magnetic Fields in the FLAPW Method

---

Name of 1st examiner: Prof. Dr. Stefan Blügel
Name of 2nd examiner: Prof. Dr. Samir Lounis

Abstract

A proposed modification of the exchange-correlation magnetic field in density functional theory is implemented into the all-electron full-potential linearized augmented-plane-wave code Fleur [1]. By removing terms from the magnetic field that stem from source contributions not found for physical ones, a recent paper [2] has shown that the prediction of Fe magnetic moments in iron pnictide materials can be improved vastly while conserving the accurate description of simpler materials. The theory justifying the idea is explored and the physicality of the modification is discussed. The interaction of the modification with different kinds of magnets is highlighted, the possible constraints in application are explained and justified and the results are compared to those from the original paper calculated via the Elk code [3]. Furthermore, the effect on the coupling parameters in a Heisenberg model is investigated to gain greater insight about how the modification works and why the improvements happen.

Contents

List of Figures

1. Introduction

Since the beginning of the 20th century and the advent of quantum physics as a fundamental theory for describing phenomena on the microscopic level, there has been an ongoing growth in the field of solid state physics and chemistry. This is true for the applications and experiments, for the amount of effects that can be successfully described by theoretical investigations and for the sheer amount of theoretical approaches that exist. None of these approaches gives the full picture that describes every single phenomenon, but instead they each have their own range of validity with respect to temperature, the number of atoms that need to be described, the overall density of the system and the type of effect that needs describing.
One of those approaches is the density functional theory (DFT) that reduces the complex many-body equation to a matter of energy optimization with respect to the ground-state density. The theory is ab initio in nature, hence it only takes the atomic structure and electron configuration of a system into account and from this can give insight into the electronic structure. It also provides a useful (although not mathematically rigorous) approximation of the band structure and density of states, allowing the theoretical description and distinction of insulators, conductors and semiconductors. While the original theory was formulated for non-magnetic systems with weak correlations that were only taken into account locally ([4], [5]) many improvements were made over the years to include collinear [6] and non-collinear magnetism [7], relativistic effects such as spin-orbit coupling [8] and even strong correlation effects by means of additional terms describing Hubbard-type interactions [9]. Due to all these extensions, DFT has become a versatile tool for first-principles calculations.
One particular field of use for DFT is the study of periodic lattices. This reduces the computational effort significantly by default, as according to the Bloch theorem, the real-space wave function can be expanded in terms of plane waves coupled to lattice-periodic functions in this case. A question distinguishing the wide range of DFT methods is, what form is an appropriate expansion of those lattice-periodic functions in terms of a basis set. In the all-electron full-potential linearized augmented plane-

wave method (FLAPW) these functions are chosen as a spherical harmonics expansion for a certain sphere around each atom and plane waves in the space separating them, leading to a pattern resembling a muffin baking sheet. One implementation of this method is the Fleur [1] code, that started as a code for the calculation of thin film systems, but has since been expanded for bulk calculations as well and has all the extensions mentioned above available.

A recent paper considering calculations with the FLAPW Elk code [3] proposed an additional modification of the magnetism that removes artifacts from the calculation of the exchange-correlation potential that lead to source terms in the resulting magnetic fields [2]. This was used to greatly improve the description of iron pnictide materials, that were shown to exhibit high-temperature superconductivity and are therefore of high interest for the understanding of the mechanisms behind it ([10], [11], [12]). In principle, the source-free modification only makes use of existing code structures like the Coulomb potential generator that is needed in every DFT code and basic derivative routines. This thesis deals with the implementation of this modification, the finer points that need to be taken into consideration when using it, its application to several materials to compare results with [2] and an investigation into how exactly the materials are affected and why the modification works the way it does.

2. Theory

The basis of all theoretical solid state physics is the many-body Hamiltonian of a system with a high number of atomic nuclei and their corresponding numbers of electrons. The full system is fundamentally too complex to be treated both analytically and numerically. Approximations need to be made to make the mathematical treatment possible [13]. The first one is often the Born-Oppenheimer or adiabatic approximation, that neglects quantum mechanical effects from the n nuclei on account of their disproportionately large mass in comparison to the electrons. They are viewed as static and only contributing a fixed external potential. This reduces the problem to an N-electron problem with the following Schrödinger equation in real space[1]:

$$H|\Psi\rangle = \left[-\sum_{i=1}^{N} \frac{1}{2}\Delta_i + \frac{1}{2} \sum_{\substack{i,j=1 \\ i \neq j}}^{N} \frac{1}{|\boldsymbol{r}_i - \boldsymbol{r}_j|} + \sum_{i=1}^{N} \sum_{j=1}^{n} \frac{Z_j}{|\boldsymbol{r}_i - \boldsymbol{R}_j|} \right] \Psi(\boldsymbol{r}_1, ..., \boldsymbol{r}_N) = E\Psi(\boldsymbol{r}_1, ..., \boldsymbol{r}_N)$$

However, this is not enough. N tends to be very large, leading to even larger dimensions of $3N$ for the wave function, while also requiring it to be anti-symmetric according to the Pauli exclusion principle. The general solution of this problem using Slater determinants as a basis is only possible for small systems and therefore unfit for the description of realistic solids. Modern ab-initio calculations are rather founded on methods from quantum chemistry, for example Hartree-Fock approximations or methods developed from them, or as is the case in this thesis, a variational ansatz known as density functional theory (DFT; see [14] for a comprehensive summary), developed initially in two papers by Hohenberg and Kohn [4] and Kohn and Sham [5].

[1] All equations in this thesis will be written in Hartree atomic units, i.e. $\hbar = m_e = e = 1$

2.1. Density Functional Theory

2.1.1. The Hohenberg-Kohn Theorem

While the N-electron wave function contains all information about the system under question, real measurable physical quantities correspond to expectation values of quantum-mechanical operators. To circumvent the superfluous amount of information gained by the wave function, it is convenient to describe these quantities in terms of the real-space electron density as given by the expectation value of an N-particle Dirac distribution [15].

$$n(\boldsymbol{r}) = \langle\Psi|\sum_{i=1}^{N}\delta(\boldsymbol{r}-\boldsymbol{r}_i)|\Psi\rangle = |\Psi(\boldsymbol{r}_1,...,\boldsymbol{r}_N)|^2$$

In [4] it is shown by Hohenberg and Kohn, that for a non-degenerate ground state two key properties hold:

a) The external potential V_{ext} (and hence the total energy E) is a unique functional of the electron density.

b) The functional $E[n]$ that delivers the ground-state energy of the system gives the lowest energy if and only if the input density is the true ground-state density $n_0(\boldsymbol{r})$.

Mathematically, this can be written as:

$$n(\boldsymbol{r}) \longleftrightarrow V_{ext}(\boldsymbol{r}),...$$

$$E[n] > E[n_0]\ \forall n(\boldsymbol{r}) \neq n_0(\boldsymbol{r})$$

Extensions to degenerate ground states have been done (see for example [16]), but are not the main focus of this thesis. The second part of the theorem implies, that the ground-state density can be found by minimizing the energy functional, leading to the condition of its functional derivative vanishing:

$$\delta E[n] = 0$$

More generally and with no initial assumption about the shape of $E[n]$, this can be redefined as:

$$E[n] = \min_{\Psi:\ n[\Psi]=n} \langle \Psi | H | \Psi \rangle$$

2.1.2. The Kohn-Sham Equations

To make the initial ideas of Hohenberg and Kohn applicable in actual calculations, the energy functional needs to be examined and categorized further. Kohn and Sham proposed a dissection into three distinct contributions.

$$E[n] = T_s[n] + U[n] + E_{xc}[n]$$

T_s is the kinetic energy of N non-interacting electrons. The Coulomb energy U is made up of the energy terms due to the external nuclear potential and the electron-electron interaction in Hartree approximation.

$$U[n] = E_{ext}[n] + E_H[n]$$
$$E_{ext}[n] = \int d^3r\ n(\boldsymbol{r}) V_{ext}(\boldsymbol{r})$$
$$E_H[n] = \frac{1}{2} \int d^3r \int d^3r'\ \frac{n(\boldsymbol{r}) n(\boldsymbol{r}')}{|\boldsymbol{r} - \boldsymbol{r}'|}$$

The exchange-correlation energy functional $E_{xc}[n]$ contains all contributions to the energy functional, that are not already contained in the non-interacting kinetic and Coulomb terms, i.e. contributions due to the interaction, meaning exchange and correlation effects between the electrons. With this separation, the kinetic term becomes less complex and reduces to a sum over the 1-particle kinetic energies.

$$T_s = \sum_{i=1}^{N} T_{s,i}$$

However, one now needs to find a way to construct this kinetic energy from the electron density instead of from the wave function. Furthermore, an exact closed form for $E_{xc}[n]$ does not exist, but a plethora of good approximations to accurately predict the structural properties and electronic structure of solids have been developed and will be discussed further in chapter 2.1.4.
To arrive at a system of equations that can be treated numerically, making an ansatz for the electron density is a common next step. In Kohn-Sham DFT, the total electron density is deconstructed into a sum of N 1-electron densities, which leads to the

definition of N 1-electron wave functions $\psi_\nu(\boldsymbol{r})$. The prefactor of 2 is accounting for the spin degeneracy of non-magnetic ground states.

$$\Psi(\boldsymbol{r}) = \sum_{\nu=1}^{N} \psi_\nu(\boldsymbol{r})$$

$$n(\boldsymbol{r}) = 2\sum_{\nu=1}^{N} |\psi_\nu(\boldsymbol{r})|^2$$

With this ansatz the kinetic energy reduces to an analytic expression and can be written as:

$$T_s[n] = -2\sum_{\nu=1}^{N} \int d^3r\ \psi_\nu^*(\boldsymbol{r})\frac{1}{2}\Delta\psi_\nu(\boldsymbol{r})$$

This form is easy to understand analytically, but not very convenient numerically, so it will be reorganized in 2.1.5. The minimization of the total energy can be reformulated into one with respect to the newly constructed $\psi_\nu(\boldsymbol{r})$. The subsidiary condition mentioned in the Hohenberg-Kohn theorem then becomes the restraint of normalized 1-electron wave functions.

$$\int d^3r\ |\psi_\nu(\boldsymbol{r})|^2 \stackrel{!}{=} 1\ \ \forall\nu \in \{1, ..., N\}$$

The theory of variational calculus states, that such a condition can be taken into account for a minimization with a Lagrange parameter ϵ_ν and the variational principle then leads to N so-called Kohn-Sham Equations, that are highly Schrödinger-like in structure.

$$H_{KS}\psi_\nu = \left[-\frac{1}{2}\Delta + V_{eff}(\boldsymbol{r})\right]\psi_\nu(\boldsymbol{r}) = \epsilon_\nu\psi_\nu$$

$$V_{eff}(\boldsymbol{r}) = V_{ext}(\boldsymbol{r}) + V_H(\boldsymbol{r}) + V_{xc}(\boldsymbol{r})$$

The effective potential $V_{eff}(\boldsymbol{r})$ consists of the external nuclear potential $V_{ext}(\boldsymbol{r})$, the Hartree potential $V_H(\boldsymbol{r})$ and the exchange-correlation potential $V_{xc}(\boldsymbol{r})$. The latter two are dependent on the total density $n(\boldsymbol{r})$, which complicates the computational effort and constitutes a self-consistency problem. The effort is albeit drastically reduced in comparison to the case of an N-electron wave function and additionally requires much less storage space, stepping down from a function with $3N$ degrees of freedom to N functions with only three dimensions.

$$V_H(\boldsymbol{r}) = \int d^3r' \, \frac{n(\boldsymbol{r}')}{|\boldsymbol{r} - \boldsymbol{r}'|}$$

$$V_{xc}(\boldsymbol{r}) = \frac{\delta E_{xc}[n(\boldsymbol{r})]}{\delta n(\boldsymbol{r})}$$

It should be noted that the Lagrange parameters ϵ_ν will often be viewed as 1-particle energies although they are not physical in that sense. They can however be related to such when considering the basic many-body theory of Fermi liquids, that describe excitations as particles with their own attributes such as position, momentum and a kinetic energy. This yields the question of the best mapping between the interacting many-body system and such a liquid of non-interacting particles. As it turns out, the Kohn-Sham mapping works very well for such a description, giving informational value to the eigenenergies, while being limited by the same condition that correlation effects are somewhat weak.

2.1.3. Magnetic systems

The theory as formulated above is enough to describe a wide class of non-magnetic systems like the very basic elemental silicon. In this case, the spin-up and spin-down electrons are not differentiated and the spin only enters as a factor 2 for the total density. Magnetic effects however can only be described with a spin-polarized ground state i.e. a non-zero ground state magnetization, which also applies to a range of materials, especially those containing elemental (anti-)ferromagnets like iron. Such is also the case for electronic systems exposed to an external magnetic field. Technically, all magnetic attributes of a system could be found with just the charge density alone, granted an appropriately exact and complicated energy functional is used, by expressing the magnetization density $\boldsymbol{m}(\boldsymbol{r})$ as a functional depending on n as well. In practice, the Hohenberg-Kohn Theorem and the resulting Kohn-Sham Equations are rather extended by $\boldsymbol{m}$ as a second variational quantity. Another possible choice to capture magnetic effects in such a way would be to instead consider the current density $\boldsymbol{j}$, which will be further discussed in chapter 2.2.1. With this second fundamental variable, the variational principle becomes:

$$E[n, \boldsymbol{m}] \geq E[n_0, \boldsymbol{m}_0]$$

Alternatively, this variation can be formulated with respect to a 2×2 density ma-

trix $\hat{\rho}(\boldsymbol{r})$ with spin-up and spin-down components [6]. Both sets of quantities are completely equivalent and can be transformed into one another. The spin-dependent form of the Kohn-Sham Equations requires the introduction of two-component Pauli wave function vectors instead of a scalar one and a 2×2 potential matrix instead of only a scalar potential. This matrix can be identified with an effective magnetic field, coupling to the vector of Pauli spin matrices $\boldsymbol{\sigma}$ in a Zeeman-like fashion.

$$\boldsymbol{\psi}_\nu(\boldsymbol{r}) = \begin{pmatrix} \psi_{\uparrow,\nu}(\boldsymbol{r}) \\ \psi_{\downarrow,\nu}(\boldsymbol{r}) \end{pmatrix}$$

$$n(\boldsymbol{r}) = \sum_{\nu=1}^{N} |\boldsymbol{\psi}_\nu(\boldsymbol{r})|^2$$

$$\boldsymbol{m}(\boldsymbol{r}) = \sum_{\nu=1}^{N} \boldsymbol{\psi}_\nu^\dagger(\boldsymbol{r}) \boldsymbol{\sigma} \boldsymbol{\psi}_\nu(\boldsymbol{r})$$

$$\left[-\frac{1}{2}\Delta + V_{eff}(\boldsymbol{r}) + \boldsymbol{\sigma} \cdot \boldsymbol{B}_{eff}(\boldsymbol{r}) \right] \boldsymbol{\psi}_\nu(\boldsymbol{r}) = \epsilon_\nu \boldsymbol{\psi}_\nu(\boldsymbol{r})$$

As in the non-magnetic scalar case for the potential, the effective magnetic field $\boldsymbol{B}_{eff}$ has several contributions. The Hartree-like contributions of the magnetization density are often neglected and the resulting field is written as:

$$\boldsymbol{B}_{eff}(\boldsymbol{r}) = \boldsymbol{B}_{ext}(\boldsymbol{r}) + \boldsymbol{B}_{xc}(\boldsymbol{r})$$

$$\boldsymbol{B}_{xc}(\boldsymbol{r}) = \frac{\delta E[n(\boldsymbol{r}), \boldsymbol{m}(\boldsymbol{r})]}{\delta \boldsymbol{m}(\boldsymbol{r})}$$

For a wide range of materials, most prominently purely ferromagnetic and anti-ferromagnetic ones, a formulation with only one magnetization density component is enough and no off-diagonal elements are needed in the potential or density matrix. That means the spin up- and down-components can be used to describe all relevant magnetic effects, where the spin up-direction is identified with the real space z-axis. The 1-particle Hamiltonian then becomes diagonal in spin space and the Schrödinger equation is decoupled into two separate non-spinpolarized ones that can be solved independently of each other. The fundamental variables are then either the total density $n(\boldsymbol{r})$ and magnetization density $m(\boldsymbol{r}) \equiv m_z(\boldsymbol{r})$ or the spin-up and spin-down densities given by:

$$n_\sigma(\boldsymbol{r}) = \sum_{\nu=1}^{N} |\psi_{\sigma,\nu}(\boldsymbol{r})|^2 = \rho_{\sigma\sigma}(\boldsymbol{r})$$

With the spin index $\sigma = \uparrow, \downarrow$. More complex magnetic structures can only be described when off-diagonal magnetism is taken into account. However, because most approximations of the exchange-correlation potential only take the two scalar quantities above as arguments, many approaches make use of local rotations of the magnetization density in real space to again calculate the two spin-up and spin-down potentials in an intermediate step and then rotate the resulting magnetic field back to the global frame. This description is sufficient to construct potentials for the case of non-collinear magnetism as well [17]. For comparison and for the sake of completeness, the necessary relation for a formulation in terms of matrices is:

$$\left[-\frac{1}{2}\Delta + \hat{V}(\boldsymbol{r})\right]\boldsymbol{\psi}_\nu(\boldsymbol{r}) = \epsilon_\nu \boldsymbol{\psi}_\nu(\boldsymbol{r})$$

With the matrices:

$$\hat{\rho}(\boldsymbol{r}) = \frac{1}{2}(\boldsymbol{I}_2 n(\boldsymbol{r}) + \boldsymbol{\sigma}\cdot\boldsymbol{m}(\boldsymbol{r})) = \frac{1}{2}\begin{pmatrix} n(\boldsymbol{r}) + m_z(\boldsymbol{r}) & m_x(\boldsymbol{r}) - i m_y(\boldsymbol{r}) \\ m_x(\boldsymbol{r}) + i m_y(\boldsymbol{r}) & n(\boldsymbol{r}) - m_z(\boldsymbol{r}) \end{pmatrix}$$

$$\hat{V}(\boldsymbol{r}) = \boldsymbol{I}_2 V_{eff}(\boldsymbol{r}) + \boldsymbol{\sigma}\cdot B_{eff}(\boldsymbol{r}) = \begin{pmatrix} V_{eff}(\boldsymbol{r}) + B_{z,eff}(\boldsymbol{r}) & B_{x,eff}(\boldsymbol{r}) - i B_{y,eff}(\boldsymbol{r}) \\ B_{x,eff}(\boldsymbol{r}) + i B_{y,eff}(\boldsymbol{r}) & V_{eff}(\boldsymbol{r}) - B_{z,eff}(\boldsymbol{r}) \end{pmatrix}$$

Where $\boldsymbol{I}_2$ is the 2×2 identity matrix. The matrix elements for the densities are given in terms of the Kohn-Sham wave functions by:

$$\rho_{\alpha\beta}(\boldsymbol{r}) = \sum_{\nu=1}^{N} \psi^*_{\beta,\nu}(\boldsymbol{r})\psi_{\alpha,\nu}(\boldsymbol{r})$$

With the spin indices $\alpha, \beta = \uparrow, \downarrow$.

2.1.4. Approximations of the Exchange-Correlation Potential

To make the theoretical concepts of DFT applicable to real materials, the exchange-correlation functional requires further investigation. A closed form in terms of the total electron density and in magnetic cases also of the magnetization density needs to be chosen, so the self consistency loop can operate. The most basic approximations harken back to the days of Hartree-Fock calculations, the Thomas-Fermi approxima-

tion or even the homogeneous electron gas. More modern variants are often found by quantum field theoretical approaches or Quantum Monte Carlo. Although more are known, there are two very common classes containing a broad collection of functionals and potentials. The first class is based on the Local Density Approximation (LDA) derived from the homogeneous electron gas, that assumes the potential to only depend on the electron density in the same point in space. Different LDA functionals only differ in the explicit parametrization of the local energy.

$$\epsilon_{xc}(\boldsymbol{r}) \approx \epsilon_{xc}(n(\boldsymbol{r})) \longrightarrow E_{xc} = \int d^3r \; n(\boldsymbol{r})\epsilon_{xc}(n(\boldsymbol{r}))$$

$$\longrightarrow V_{xc}(\boldsymbol{r}) = \epsilon_{xc}(n(\boldsymbol{r})) + n(\boldsymbol{r})\frac{\delta\epsilon_{xc}(n(\boldsymbol{r}))}{\delta n(\boldsymbol{r})}$$

The generalization to spin-polarized systems is straightforward in the sense, that $|\boldsymbol{m}(\boldsymbol{r})|$ enters as a second variable into the exchange-correlation energy density and the exchange-correlation magnetic field will be parallel to the magnetization density for every point in space. It can be calculated as:

$$\boldsymbol{B}_{xc}(\boldsymbol{r}) = n(\boldsymbol{r})\frac{\delta\epsilon_{xc}(n(\boldsymbol{r}), |\boldsymbol{m}(\boldsymbol{r})|)}{\delta|\boldsymbol{m}(\boldsymbol{r})|}\hat{\boldsymbol{m}}(\boldsymbol{r})$$

This form of DFT is known as spin-density functional theory (SDFT). The simple form for the magnetic field is the reason the Local Spin Density Approximation (LSDA) can easily be applied to systems with non-collinear magnetism. LDA functionals were shown over the years to produce very accurate results in many cases, with the general caveat that the approximation tends to overbind structures, meaning that it will mostly underestimate lattice constants. Another shortcoming is that it predicts iron to form a non-magnetic face-centered cubic structure instead of the ferromagnetic body-centered cubic one it is known to have in reality [18]. There is, however, another important class of functionals that also take into account the spatial derivatives of the densities. The Generalized Gradient Approximation (GGA) for non-spinpolarized systems tries to improve the description by not neglecting non-localities in $\epsilon_{xc}(\boldsymbol{r})$ in the sense that the spatial gradient of the electron density is introduced as a second variable.

$$\epsilon_{xc}(\boldsymbol{r}) \approx \epsilon_{xc}(n(\boldsymbol{r}), \nabla n(\boldsymbol{r}))$$

GGA functionals differ far more between different parametrizations, as the addi-

tional question of exactly how to incorporate the gradients arises. GGA functionals yield improved results for a wide class of non-magnetic systems, mostly curing the shortcomings highlighted above while instead tending to underbind structures a little. But the proper description of magnetism becomes more complicated with GGA in the case of non-collinear magnetism. It is not trivial to analyze, which gradient of which quantity should enter the energy density in which way[2]. The inherently parallel magnetization density and magnetic field from LSDA are no longer given and the space of possible resulting parametrizations is vast. The Fleur code partially circumvents this problem by explicitly rotating the magnetization density in each point of space into the positive z-axis before calculating $\hat{V}_{xc}$ and rotating the resulting potential back afterwards. In this approach, the gradient of the absolute value of the magnetization density is used[3]. This constitutes a second layer of approximation to the functional.

2.1.5. Calculating the total energy

For several types of calculations, for example when calculating the optimized structure of a crystal, information about the total energy of the system is needed. One relevant term was neglected in previous chapters, namely the contribution from the ion-ion interaction causing forces that can contract or expand the system and shift atoms around. It is, of course, similar in form to the electron-electron and electron-ion interaction.

$$E_{ion} = \frac{1}{2} \sum_{\substack{j,j'=1 \\ j \neq j'}}^{n} \frac{Z_j Z_{j'}}{|\boldsymbol{R}_j - \boldsymbol{R}_{j'}|}$$

Rearranging and replacing the kinetic energy term, that is not very handy for calculations in real space, by terms gained from the Kohn-Sham equations like the energy eigenvalues the following final form arises:

$$E[n,m] = \sum_{\nu=1}^{N} \epsilon_\nu - \int d^3r\, n(\boldsymbol{r}) V_{xc}(\boldsymbol{r}) - \int d^3r\, \boldsymbol{m}(\boldsymbol{r}) \cdot \boldsymbol{B}_{xc}(\boldsymbol{r}) - \frac{1}{2} \int d^3r \int d^3r' \, \frac{n(\boldsymbol{r}) n(\boldsymbol{r}')}{|\boldsymbol{r} - \boldsymbol{r}'|}$$

[2]Case in point: While finishing this thesis, the method with which the gradient is evaluated in Fleur was changed from the one given in equation (27) to equation (28) from [7].
[3]I.e. the calculation scheme according to equation (27).

$$+ \int d^3r \; n(\boldsymbol{r})\epsilon_{xc}(n(\boldsymbol{r}), |\boldsymbol{m}(\boldsymbol{r})|) + \frac{1}{2} \sum_{\substack{j,j'=1 \\ j \neq j'}}^{n} \frac{Z_j Z_{j'}}{|\boldsymbol{R}_j - \boldsymbol{R}_{j'}|}$$

In principle, this is the quantity that needs to be minimized with respect to the densities in a self-consistent way.

2.1.6. The self-consistent field cycle in DFT

As alluded to above, modern DFT calculations solve the Kohn-Sham Equations self-consistently. This self-consistent field (SCF) cycle begins with an input density and iteratively converges it to a final result given by the condition that the density changes less than a preset ϵ in the last iteration. For the Fleur code specifically, there are a set of additional steps after the generation of the potential from the density that are listed here and explained in detail in the chapter on computational details. In most methods, a basis in which to expand the wave functions, densities and potentials needs to be chosen. As periodic solids are very often the system under consideration, plane waves are the most basic choice and the notation using reciprocal lattice vectors $\boldsymbol{G}$ and Bloch vectors $\boldsymbol{k}$ for the resulting matrix elements stems from this approach:

$$\varphi_{\boldsymbol{G}}(\boldsymbol{k}, \boldsymbol{r}) = \frac{1}{\sqrt{\Omega}} e^{i(\boldsymbol{k}+\boldsymbol{G})\cdot\boldsymbol{r}}$$

$$H^{\boldsymbol{G}'\boldsymbol{G}}(\boldsymbol{k}) = \langle \varphi_{\boldsymbol{G}'}(\boldsymbol{k}) | H_{KS} | \varphi_{\boldsymbol{G}}(\boldsymbol{k}) \rangle = \int d^3r \; \varphi^*_{\boldsymbol{G}'}(\boldsymbol{k}, \boldsymbol{r}) H_{KS} \varphi_{\boldsymbol{G}}(\boldsymbol{k}, \boldsymbol{r})$$

After the eigenvalues and eigenvectors are calculated for each band index ν, the Fermi energy is calculated from the requirement of particle number conservation and all wave functions with energies below the Fermi energy make up the new density calculated from the present iteration. The input and output density are mixed together to a degree pre-determined by a mixing parameter α. In the most basic case of simple mixing, a method with linear convergence, the mixed density is determined as:

$$n^{m+1} = (1 - \alpha) n^m + \alpha F\{n^m\}$$

F is the mix vector representing the output density of the current iteration, driving the density to the minimum. As this method is very stable for small α, but very slow, different mixing schemes based on Newton-Raphson and Quasi-Newton methods are preferred, but these will not be explained here in detail. The resulting quantity

constitutes the input for the next iteration. In the Fleur framework, after the convergence of the density, optional structure optimizations can be performed. For this, the forces acting on each atom are calculated as derivatives of the total energy and the atoms are displaced by a small amount accordingly to relax the structure. SCF-calculations and relaxations are done alternately until the forces are converged to a preset distance ϵ_{Force} from zero. This corresponds to the idea of Born-Oppenheimer dynamics, in contrast to Car-Parrinello schemes, that converge both the density ad the forces simultaneously. Figure 2.1 highlights the necessary steps for an SCF loop without structure relaxations. The details for its execution in the FLAPW method are described in chapter 2.4.

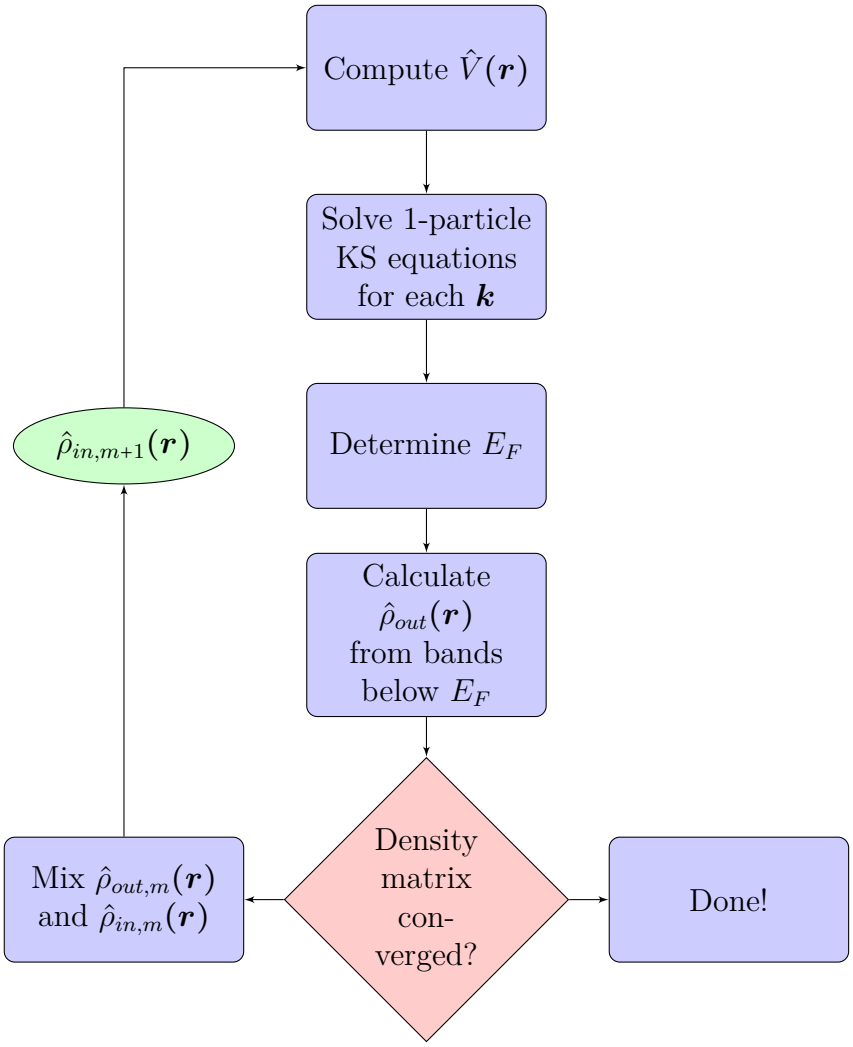

Figure 2.1.: Flowchart of the basic DFT SCF loop (c.f. [19])

2.2. Source-Free magnetism

The treatment of magnetism within an ab-initio framework is a challenging task. The multitude of theoretical entry points all bring their own qualities and difficulties to the table. In the previous chapters, the method of Spin-Density Functional Theory was proposed. The magnetization density and magnetic field are extracted from a spin-polarized density with up- and down components. From this, a non-collinear density either results from gradient terms in GGA approaches or can be found by rotating a collinear field from a rotated local density back to a global frame in both LSDA and GGA theories. This chapter introduces another approach based on current-density functional theory (CDFT) and highlights a possible transition between the two for certain cases [20]. From this transition, a method to remove magnetic fields resulting from source-terms that appear as artifacts of the exchange-correlation functional is proposed, that was used by Sharma et al. [2] to great avail when analyzing pnictide materials, improving the description of their internal magnetic moments drastically when compared to the normal non-collinear case.

2.2.1. Current-Density Functional Theory

In the original formulation of CDFT [21], the SDFT Hamiltonian is modified by two extra terms. The first describes the coupling of an external vector potential $\boldsymbol{A}$ to a diamagnetic current density $\boldsymbol{j}_d$. The second term corresponds to a quadratic dependency on that external potential. The treatment applied in the following does not rely on this external potential but rather assumes $\boldsymbol{A} = 0$ and starts from an identity shown in [20] that establishes a direct relation between SDFT and CDFT functionals for the case of vanishing peripheral fields and under the initial assumption of a finite system. However, the condition of vanishing fields can be replaced with the assumption of a periodic system, making boundary terms vanish when performing integration by parts. The idea is as follows, starting from the total energy functional in SDFT.

$$E_{V_{ext},\boldsymbol{B}_{ext}}[n,\boldsymbol{m}] = T_s[n]+E_H[n]+E_{xc}[n,\boldsymbol{m}]+\int d^3r\, n(\boldsymbol{r})V_{ext}(\boldsymbol{r})+\int d^3r\, \boldsymbol{m}(\boldsymbol{r})\cdot\boldsymbol{B}_{ext}(\boldsymbol{r})$$

Assuming the external magnetic field is physical, it must be the rotation of an external vector field $\boldsymbol{A}$ and integration by parts yields:

$$\int d^3r\ \boldsymbol{m}(\boldsymbol{r}) \cdot \boldsymbol{B}_{ext}(\boldsymbol{r}) = \int d^3r\ \boldsymbol{A}_{ext}(\boldsymbol{r}) \cdot \nabla \times \boldsymbol{m}(\boldsymbol{r})$$

Instead of the magnetization density $\boldsymbol{m}$, its curl now appears as a fundamental variable in the functional. This curl can be identified with the spin-current density. This requires the reformulation of the exchange-correlation energy into a new functional $\tilde{E}_{xc}[n, \nabla \times \boldsymbol{m}]$ as well. From this one can derive a corresponding new exchange-correlation magnetic field.

$$\tilde{\boldsymbol{B}}_{xc}(\boldsymbol{r}) = \frac{\delta E[n(\boldsymbol{r}), \nabla \times \boldsymbol{m}(\boldsymbol{r})]}{\delta \boldsymbol{m}(\boldsymbol{r})} = \int d^3r'\ \frac{\delta(\nabla \times \boldsymbol{m}(\boldsymbol{r}'))}{\delta \boldsymbol{m}(\boldsymbol{r})} \frac{\delta E[n(\boldsymbol{r}), \nabla \times \boldsymbol{m}(\boldsymbol{r})]}{\delta(\nabla \times \boldsymbol{m}(\boldsymbol{r}'))}$$

$$= \int d^3r'\ \delta(\boldsymbol{r} - \boldsymbol{r}') \nabla \times \frac{\delta E[n(\boldsymbol{r}), \nabla \times \boldsymbol{m}(\boldsymbol{r})]}{\delta(\nabla \times \boldsymbol{m}(\boldsymbol{r}'))}$$

$$= \int d^3r'\ \delta(\boldsymbol{r} - \boldsymbol{r}') \nabla \times \boldsymbol{A}_{xc}(\boldsymbol{r}') = \nabla \times \boldsymbol{A}_{xc}(\boldsymbol{r})$$

The functional derivative in the integrand is identified as an exchange-correlation vector potential. As the magnetic field is its curl, it is source-free by construction. So the field can be chosen to be source-free under the condition that the variation is done with respect to the spin-current density. The curl of the resulting magnetization density is the same as in the unmodified SDFT case, but the magnetization may differ up to a curl-free function, i.e. the gradient of a scalar function $f(\boldsymbol{r})$.

$$\boldsymbol{m}(\boldsymbol{r}) \longrightarrow \boldsymbol{m}(\boldsymbol{r}) + \nabla f(\boldsymbol{r})$$

That means the curl is exact, while the magnetization density itself is not. However, the total magnetic moment per unit cell $\boldsymbol{M}$ and integrated moments over volumes with vanishing $\boldsymbol{m}$ at the boundaries are conserved, as the integral over the gradient vanishes.

2.2.2. Manually projecting out source terms

While CDFT yields a source-free description of magnetism, its major downside is the lack of proper functionals to use it with and calculate an exchange-correlation vector field $\boldsymbol{A}_{xc}$. Not many exist, that are more than the most basic LDA approach. So the question arises, whether one can achieve some of the key advantages of CDFT within

an SDFT framework. To make the theoretical and mathematical effort more manageable, the Helmholtz theorem from classical electrodynamics was applied instead by Sharma et al. It states, that every real-space vector field (that is twice differentiable) can be decomposed into a curl-free and a source-free part, where the first one can be written as the real-space gradient of a scalar potential ϕ and the second one as the real-space curl of a vector potential $\boldsymbol{A}$. That means it is possible to construct the source density of a given field by calculating its gradient. This source density enters the Poisson equation to find the aforementioned scalar potential.

$$\Delta\phi = -4\pi\nabla \cdot \boldsymbol{B}_{xc}$$

The potential can be calculated in much the same way as the Coulomb potential in the normal SCF loop, if the divergence of the magnetic field is represented the same way as the normal charge density that enters the Poisson equation solver. From the gradient of this potential one can then construct a correction field and from this a new magnetic field, that is source-free by construction.

$$\tilde{\boldsymbol{B}}_{xc} = \boldsymbol{B}_{xc} + \frac{1}{4\pi}\nabla\phi$$

The scalar part V_{eff} of the potential is not modified by this procedure. This treatment gives the magnetic field a set of additional properties when compared to the unmodified one.

a) $\tilde{\boldsymbol{B}}_{xc}$ becomes necessarily non-local as it is obtained by solving the non-local Poisson Equation, even if an LSDA functional was used initially and no gradients were taken into account.

b) $\tilde{\boldsymbol{B}}_{xc}$ becomes necessarily non-collinear, even if the initial formulation was not. As a consequence, the cross product of the magnetization density and magnetic field is no longer 0 as it is by construction in unmodified LSDA and GGA.

$$\boldsymbol{m}(\boldsymbol{r}) \times \boldsymbol{B}_{xc}(\boldsymbol{r}) \neq 0$$

The modification enters the SCF loop after the standard potential generation as a finalizing option. Additionally, the authors of the original paper propose an additional modification. The magnetization density entering E_{xc} from which the magnetic field is calculated is scaled up by a factor s. The same goes for the resulting magnetic

field afterwards. This is done to enhance the spin-splitting and to keep the functional variational. The parameter was chosen to optimize the magnetic moment per atom for two materials and then applied to all others that were studied. It was observed to be roughly universal across various materials, although dependent on the chosen functional. This dependency will be explored further in the following chapters and verified in 3.2.

2.3. The generalized Heisenberg model

A very basic model often used in conjunction with DFT and its results is the so-called classical Heisenberg model that treats the atoms as interacting fixed magnetic moments. The associated Hamiltonian reduces the complex interaction terms to couplings between these moments and allows to gain greater insight about the preferred magnetic order in a material. The model is, in its most basic form, only dependent on a coupling parameter J between nearest neighbours, i.e. directly adjacent atoms in the lattice, and the magnetic moment related to the atomic spins. There are, however, generalized versions that allow for coupling between next-nearest neighbours or even higher orders. Other models also take couplings of more than two atoms with vectorial or tensorial couplings into account. Such couplings are important to describe anisotropic magnetic configurations and to explain why they form. Chapter 5.2 will deal with Heisenberg coupling parameters up to the second order to investigate and explain the exact effect that the source-free modification has on the magnetic order of a simple structure with a single type of atom. The generalized Hamiltonian is:

$$H_{Heisenberg} = -\sum_{i,j} J_{i,j} \boldsymbol{S}_i \cdot \boldsymbol{S}_j$$

For a next-nearest neighbour system (abbreviated as n.-n. n.) this reduces to two terms for the immediate coupling between adjacent atoms (conventionally written as <i,j>) and second order contributions (written here as $<< i, j >>$).

$$H_{n.-n.n.} = -J_1 \sum_{<i,j>} \boldsymbol{S}_i \cdot \boldsymbol{S}_j - J_2 \sum_{<<i,j>>} \boldsymbol{S}_i \cdot \boldsymbol{S}_j$$

To gain insight about the couplings from a converged DFT calculation, one needs to associate the total energy of the unit cell with an energy contribution from the Heisenberg term. The parameters can then be gained by linear combinations of energies from at least m different (anti-)ferromagnetic orderings of the same structure for $m-1$ couplings. The m-th linearly independent parameter will always be a reference energy E_0 that contains all energy terms not modeled by the Heisenberg interaction.

$$E_{DFT} = E_0 - J_1 \sum_{<i,j>} \boldsymbol{S}_i \cdot \boldsymbol{S}_j - J_2 \sum_{<<i,j>>} \boldsymbol{S}_i \cdot \boldsymbol{S}_j$$

2.4. Specifics of the FLAPW method

Based on the fundamental theory from the previous chapters, the question now arises how to execute the self-consistency loop in particular. To solve the Kohn-Sham equations for each orbital, a suitable basis needs to be chosen that can accurately describe the Kohn-Sham wave functions in the solid. From the choice of this basis, one gets a set of properties to use and additionally new questions and problems that need to be dealt with concerning the explicit generation of potentials, the construction of the Kohn-Sham Hamiltonian and the solution of the eigenvalue problem it yields. The Fleur code [1] is based on the all-electron full-potential linearized augmented plane wave (FLAPW) approach, that is a highly thorough and precise approach to the study of electronic structure and magnetic phenomena that other methods are frequently benchmarked against. There are no assumptions made about the shape of the potential and no pseudopotentials are used. Relativistic effects can also be taken into account on several levels [22]. Furthermore, the basis is systematically extendable to ensure convergence with respect to the representation [23].

2.4.1. Steps towards FLAPW

Actual calculations to determine the properties of real materials are frequently done for periodic solids. According to the Bloch Theorem, the basis from which the wave function and by extension the Kohn-Sham orbitals are built can then be chosen as the product of periodic trial wave functions and plane waves with a wave vector $\boldsymbol{k}$. The most basic choice for the periodic functions would be plane waves, making various calculations within the cycle very easy.

$$\psi_\nu(\boldsymbol{k},\boldsymbol{r}) = \sum_{|\boldsymbol{k}+\boldsymbol{G}|\leq K_{max}} c^{\boldsymbol{G}}_{\boldsymbol{k},\nu}\varphi_{\boldsymbol{G}}(\boldsymbol{k},\boldsymbol{r})$$

Where $\boldsymbol{k}$ is the Bloch wave vector, Ω is the volume of the unit cell, $\boldsymbol{G}$ are the reciprocal lattice vectors and K_{max} is the maximum absolute value up to which the plane waves are taken into account. $\psi_\nu(\boldsymbol{k},\boldsymbol{r})$ are the Kohn-Sham wave functions for each band and $c^{\boldsymbol{G}}_{\boldsymbol{k},\nu}$ are the plane wave coefficients that constitute them. In this basis, problems arise when calculating properties for the atomic regions. While plane waves do a good job of describing smooth periodic functions, they are not well suited for capturing the radial and divergent nature of the electrons near a core that lead to heavy oscillations of the resulting wave functions and therefore require impractically

high cutoffs for the set of $\boldsymbol{G}$. The first improvement over this are Slater's Augmented Plane Waves (APW) [24], that take a different basis of radial and angular functions to describe the electrons within a certain radius of each atomic core. This leads to a structure resembling a muffin baking sheet for the unit cell, hence the atomic regions are commonly referred to as Muffin Tins (MT) as sketched in figure 2.2. The remaining part of the cell is called the interstitial region. The basis functions then take the form:

$$\varphi_{\boldsymbol{G}}(\boldsymbol{K},\boldsymbol{r}) = \begin{cases} \frac{1}{\sqrt{\Omega}} e^{i(\boldsymbol{K}+\boldsymbol{G})\cdot\boldsymbol{r}} & \boldsymbol{r} \in Interstitial \\ \sum_{lm} A_{lm}^{\mu\boldsymbol{G}}(\boldsymbol{K}) u_l(r_\mu) Y_l^m(\hat{\boldsymbol{r}}_\mu) & \boldsymbol{r} \in MT^\mu \end{cases}$$

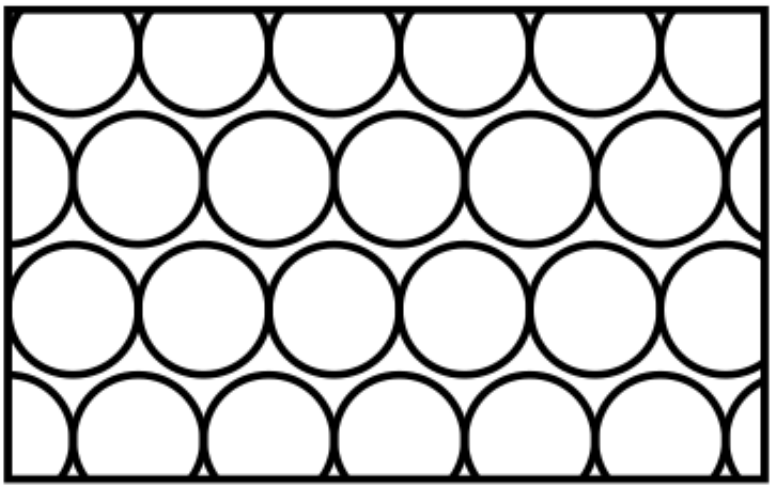

Figure 2.2.: Visualization of the space separation in APW methods with Muffin Tins (as found in [19])

Where the coefficients $A_{lm}^{\mu\boldsymbol{G}}(\boldsymbol{K})$ are fixed by the condition that the basis needs to be continuous at the MT boundaries and $\boldsymbol{r}_\mu = \boldsymbol{r} - \boldsymbol{R}_\mu$ with $\boldsymbol{R}_\mu$ the center of MT^μ. $u_l(r)$ is the regular solution of the spherical Schrödinger equation given by:

$$\left[-\frac{\hbar^2}{2m_e}\partial_r^2 + \frac{\hbar^2}{2m_e}\frac{l(l+1)}{r^2} + V(r) - E_l\right] r u_l(r) = 0$$

With the spherical component of the potential $V(r)$ and the energy parameter E_l. With a fixed E_l that only enters into the construction of the basis, a standard secular equation for the band energies would arise. It turns out that is approach does not yield enough variational freedom to find an appropriate ground state. For that the E_l need to be set to the band energies, which can then no longer be obtained by simply

diagonalizing the Hamiltonian. The energy parameters $E_l(\boldsymbol{k}, \nu)$ are then dependent on the Bloch wave vector and the band index. The computational problem becomes nonlinear and thus highly resource-intensive. The choice of E_l also becomes even more difficult when more than a spherically averaged approximation of the MT-potential is used, as the band energies are then no longer the optimal choice. Another difficulty is the asymptote problem. When $u_l(R_{MT^\mu})$ becomes zero, the radial functions and plane waves become decoupled and the coefficients can no longer be matched. For an extensive discussion of the APW method, consult [24] or [25].
To cure the lack of variational freedom, Andersen [26] proposed the linearization of the spherical Schrödinger equation around the energy parameters and added the energy derivatives of u_l to the basis set, creating the Linearized Augmented Plane Wave (LAPW) approach. This way, the E_l are no longer required to match the band energies. The corresponding Taylor series with respect to the energy ϵ reads:

$$u_l(\epsilon, r) = u_l(E_l, r) + \dot{u}_l(E_l, r)(\epsilon - E_l) + O[(\epsilon - E_l)^2]$$

The linearization error [27] is of quadratic order in ϵ and therefore in the wave function, leading to an error of $O[(\epsilon - E_l)^4]$ in the calculated band energies. This leads to a good description of the wave function across a broad range of energy parameters and makes choosing a single set for the whole valence band viable in most cases. There are ways to cover an even broader range like simply using additional sets of energy parameters for different energy windows (instead of only differentiating between core and valence states). This means different basis functions for different energies. The Fleur code instead relies on the extension of the basis by another type of function by adding local orbitals to the already existing radial functions and derivatives. They will be discussed below.
The LAPW approach brings its own merits and problems. The basis functions now read:

$$\varphi_{\boldsymbol{G}}(\boldsymbol{K}, \boldsymbol{r}) = \begin{cases} \frac{1}{\sqrt{\Omega}} e^{i(\boldsymbol{K}+\boldsymbol{G})\cdot\boldsymbol{r}} & \boldsymbol{r} \in Interstitial \\ \sum_{lm}(A_{lm}^{\mu\boldsymbol{G}}(\boldsymbol{K})u_l(r_\mu, E_l) + B_{lm}^{\mu\boldsymbol{G}}(\boldsymbol{K})\dot{u}_l(r_\mu, E_l))Y_l^m(\hat{\boldsymbol{r}}_\mu) & \boldsymbol{r} \in MT^\mu \end{cases}$$

For even greater variational freedom, as mentioned above, this equation is frequently augmented by a third additive term $C_{lm}^{\mu\boldsymbol{G}}(\boldsymbol{K})u_{LO}(r_\mu)$ representing the local orbitals, leading to the LAPW+LO approach. The new coefficients $B_{lm}^{\mu\boldsymbol{G}}(\boldsymbol{K})$ (and

$C_{lm}^{\mu \boldsymbol{G}}(\boldsymbol{K})$) are fixed by the additional requirement of continuous derivatives at the MT-boundaries (while the local orbitals are fixed to 0 there). The radial functions are normalized according to:

$$\langle u_l | u_l \rangle = \int_0^{R_{MT}} dr\ r^2 u_l^2(r) = 1$$

From this the orthogonality of u_l and $\dot{u}_l$ can easily be constructed by taking the energy derivative. The energy derivative of the radial Schrödinger equation also gives an equation for the additional basis functions.

$$\left[-\frac{\hbar^2}{2m_e} \partial_r^2 + \frac{\hbar^2}{2m_e} \frac{l(l+1)}{r^2} + V(r) - E_l \right] r\dot{u}_l(r) = r u_l(r)$$

As the basis functions are linear combinations of the different radial constituents, they do not form an orthonormal set. They are, however, mostly orthogonal to the core states [14], making their mixed contributions to the Eigenvalue problem vanish. The matrix elements of the valence states are non-zero in general.
The advantages of the LAPW approach compared to APW are mostly obvious by construction. One regains the ability to calculate the band energies by the diagonalization of a single Hamiltonian like in the case of pure plane waves and the asymptote problem at the MT-boundaries of APW is cured by the inclusion of the derivatives. Additionally, the shape of the potential is not required to assume any particular shape but can be acquired self-consistently and without restriction, which will be discussed in the following chapter on FLAPW (Full-Potential Linearized Augmented Plane Waves). As a caveat, it should be noted that LAPW requires an increased amount of plane waves when compared to APW, as the radial basis couples to the interstitial via the coefficients $A_{lm}^{\mu \boldsymbol{G}}(\boldsymbol{K})$ and $B_{lm}^{\mu \boldsymbol{G}}(\boldsymbol{K})$. The number of radial functions u_l and $\dot{u}_l$ that can be varied independently of each other is at most the same as the number of plane waves provided for the calculation. Hence, enough plane waves must be chosen to ensure that the amount suffices for the additional description by the $\dot{u}_l$.

2.4.2. The FLAPW approach and its representations

Most early APW approaches made use of pseudopotentials within the muffin tins. The (L)APW method in contrast enabled a description of spherical potentials there, but most studies still assumed the shape of the corresponding interstitial potential to be constant (baring exceptions like [28]) and angular effects were still neglected. This

constitutes the following potential:

$$V(\boldsymbol{r}) = \begin{cases} V_I & \boldsymbol{r} \in Interstitial \\ V_{MT^\mu}(r_\mu) & \boldsymbol{r} \in MT^\mu \end{cases}$$

Both these shape approximations are no longer made in the FLAPW method developed in [29] and [30]. Instead, the interstitial potential is again written as a plane-wave expansion in the interstitial region and now additionally as a spherical harmonics expansion in the MTs.

$$V(\boldsymbol{r}) = \begin{cases} \sum_{\boldsymbol{G}} V_I^{\boldsymbol{G}} e^{i\boldsymbol{G}\cdot\boldsymbol{r}} & \boldsymbol{r} \in Interstitial \\ \sum_{lm} V_{MT^\mu}^{lm}(r_\mu) Y_l^m(\hat{\boldsymbol{r}}_\mu) & \boldsymbol{r} \in MT^\mu \end{cases}$$

The calculation of this potential will be discussed in 2.4.4 and relies on a corresponding description of the real-space density in the same representation.

$$\rho(\boldsymbol{r}) = \begin{cases} \sum_{\boldsymbol{G}} \rho_I^{\boldsymbol{G}} e^{i\boldsymbol{G}\cdot\boldsymbol{r}} & \boldsymbol{r} \in Interstitial \\ \sum_{lm} \rho_{MT^\mu}^{lm}(r_\mu) Y_l^m(\hat{\boldsymbol{r}}_\mu) & \boldsymbol{r} \in MT^\mu \end{cases}$$

In proper DFT calculations, the symmetry of the lattice is also taken into account. I.e., the representation changes from pure plane waves and spherical harmonics to a new basis of functions, split between the so-called stars in the interstitial region and lattice harmonics in the spheres. The stars are constructed by summing all plane waves that result from one representative $\boldsymbol{G}_s$ by application of the N_s symmetry transformations $T = \{R|\boldsymbol{\tau}\}$ of a lattice space group, consisting of rotations described by the matrix R and translations by the vector $\boldsymbol{\tau}$.

$$\Phi_s(\boldsymbol{r}) = \frac{1}{N_s} \sum_T e^{iR\boldsymbol{G}_s\cdot(\boldsymbol{r}-\boldsymbol{\tau})}$$

This way, all plane waves that are equivalent are combined in a single star. In the spheres, the point group of the atoms symmetries needs to be taken into account instead, leading to different harmonics for different atoms in a given structure. The combination into lattice harmonics K_L is:

$$K_L^\mu(\hat{\boldsymbol{r}}_\mu) = \sum_m c_L^{m,\mu} Y_{l(L)}^m(\hat{\boldsymbol{r}}_\mu)$$

With the expansion coefficients $c_L^{m,\mu}$. In principle, these coefficients each combine two spherical harmonics with the same l into one real spherical harmonic (i.e. terms

$\sim e^{\pm i\varphi}$ into sine and cosine terms) and eliminate angular dependencies, that do not fit the symmetry of the system. It should be noted, that the application of the source-free modification in the Fleur code uses intermediate quantities with reduced symmetry. The symmetrized functions are constructed for the initial symmetry from the crystal structure and to avoid conflicts between iterations, all calculations are done without any symmetry operations besides the identity matrix. The Fleur code also extends the basis to a third section, the vacuum, for the calculation of thin film systems. As this thesis focuses on bulk properties, this will not be highlighted further.

2.4.3. Calculating the divergence of the magnetic field

This short chapter highlights the execution of derivatives in the particular FLAPW basis chosen for Fleur and the problems that can arise when calculating them. Symmetrizations will be neglected for the moment and the assumed representations are products of radial functions and spherical harmonics in the MTs and plane waves in the interstitial region. That means, the magnetic field takes the same expanded form as the charge density and potential in the previous section. The summation index j represents the three cartesian directions of space.

$$\boldsymbol{B}(\boldsymbol{r}) = \begin{cases} \sum_{\boldsymbol{G}} \boldsymbol{B}_I^{\boldsymbol{G}} e^{i\boldsymbol{G}\cdot\boldsymbol{r}} & \boldsymbol{r} \in Interstitial \\ \sum_{lm,j} \hat{\boldsymbol{e}}_j B_{MT^\mu}^{lm,j}(r_\mu) Y_l^m(\hat{\boldsymbol{r}}_\mu) & \boldsymbol{r} \in MT^\mu \end{cases}$$

For use with the pre-programmed Poisson equation solver as described in 2.2.2, the divergence of this magnetic field needs to be written in the same form as well. To do so, the differentiation is executed separately for both regions. The derivatives in the MTs are calculated according to a formula from [31]. The differentiation is first executed in a natural coordinate representation corresponding to the spherical multipole expansion at $l = 1$ and then transformed back to the cartesian basis via a transformation matrix $\boldsymbol{T}$. The natural basis is indicated by the m' index, the cartesian one again by j. The radial functions for the spherical harmonics expansion then take the following form:

$$(\nabla \cdot \boldsymbol{B})_{MT^\mu}^{lm}(r_\mu) = \sqrt{\frac{4\pi}{3}} \sum_{j=1}^{3} \sum_{m'=-1}^{1} \hat{\boldsymbol{e}}_j \boldsymbol{T} \hat{\boldsymbol{e}}_{m'} (-1)^{m'}$$

$$\cdot \left[\left(\frac{d}{dr} B_{MT^\mu}^{l+1,m+m',j}(r_\mu) + (l+2) \frac{B_{MT^\mu}^{l+1,m+m',j}(r_\mu)}{r} \right) G_{l,l+1,1}^{m,m+m',-m'} \right.$$

$$+\left(\frac{d}{dr}B_{MT^\mu}^{l-1,m+m',j}(r_\mu)-(l-1)\frac{B_{MT^\mu}^{l-1,m+m',j}(r_\mu)}{r}\right)G_{l,l-1,1}^{m,m+m',-m'}\Bigg]$$

The factors $G_{l_1,l_2,l_3}^{m_1,m_2,m_3}$ that appear in the summation are the Gaunt coefficients. The coefficients and the transformation matrix are defined as follows:

$$\boldsymbol{T} = \frac{1}{\sqrt{2}}\begin{pmatrix} 1 & 0 & -1 \\ -i & 0 & -i \\ 0 & \sqrt{2} & 0 \end{pmatrix}$$

$$G_{l_1,l_2,l_3}^{m_1,m_2,m_3} = \int d\Omega\ Y_{l_1}^{m_1,*}(\Omega)Y_{l_2}^{m_2}(\Omega)Y_{l_3}^{m_3}(\Omega)$$

The rows of $\boldsymbol{T}$ are counted from 1 to 3 while the columns are numbered as -1, 0 and 1. Considering that the potential generation conserves which lm-channels are occupied (2.4.4) and another differentiation is done for the gradient afterwards, it is easy to see that the procedure partially scatters contributions from each l into the channels with an orbital quantum number of $l \pm 2$. This does not per se lead to a reduction in symmetry for the system, but the intermediate quantities like the divergence used as a source density do not have the same symmetry as the original magnetic field, which needs to be taken into account by not using symmetrized expansions of the charge density and potential to begin with. Additionally, as there is a cutoff of l_{max} for all MT quantities, the correction to the highest components is not necessarily accurate. The derivatives in the interstitial region are readily available, as they only amount to a multiplication with the wave vector.

$$(\nabla \cdot \boldsymbol{B})_{\boldsymbol{G}} = i\ \boldsymbol{G} \cdot \boldsymbol{B}_{\boldsymbol{G}}$$

This simple derivation is also only possible when neglecting the construction of stars, which becomes obvious when looking at the particular form of a star, that takes several $\boldsymbol{G}$ into account.

2.4.4. Potential generation in the FLAPW basis

The all-electron full-potential method of DFT became feasible largely thanks to a proper way of solving the Poisson Equation for a charge density given in the representation from 2.4.2 [32]. A completely localized charge density in the MTs could be used to construct the potential in a spherical multipole expansion, the interstitial

part and the resulting transition between two mathematical expressions complicate the situation and make the resulting boundary value problem more difficult to handle. The density is first split up into these two contributions.

$$\rho(\boldsymbol{r}) = \rho_I(\boldsymbol{r})\Theta(\boldsymbol{r} \in I) + \sum_{\mu} \rho_\mu(\boldsymbol{r})\Theta(\boldsymbol{r} \in MT^\mu)$$

The indicator functions $\Theta(\boldsymbol{r} \in A)$ are either 1 or 0, depending on whether the point $\boldsymbol{r}$ is within the volume A. This charge density can be replaced by a new one when taking into account, that the potential in the interstitial is fully determined by the interstitial density and the multipoles of its MT densities, not the explicit shape of these densities themselves. The MT-densities are hence replaced by smooth pseudo-densities with equivalent multipoles to ensure fast convergence of the corresponding Fourier representation of the interstitial potential.

$$\tilde{\rho}(\boldsymbol{r}) = \rho_I(\boldsymbol{r})\Theta(\boldsymbol{r} \in I) + \sum_{\mu} \tilde{\rho}_\mu(\boldsymbol{r})\Theta(\boldsymbol{r} \in MT^\mu)$$

The solution of the Poisson Equation for this density yields an interstitial potential, that accurately describes the potential outside the MTs.

$$V_I(\boldsymbol{r}) = \sum_{\boldsymbol{G}\neq\boldsymbol{0}} \frac{4\pi\tilde{\rho}(\boldsymbol{G})}{\boldsymbol{G}^2} e^{i\boldsymbol{G}\cdot\boldsymbol{r}}$$

The corresponding MT-potentials are then the solutions of the Poisson Equation with the exact MT-densities and the interstitial potential as Dirichlet boundary values. In the spherical harmonics expansion, the radial parts of the potentials can be written as:

$$V_\mu^{lm}(r) = \frac{4\pi}{2l+1} \int_0^{R_{MT^\mu}} dr' r'^2 \rho_\mu^{lm}(r') \frac{r_<^l}{r_>^{l+1}} \left(1 - \left(\frac{r_>}{R_{MT^\mu}}\right)^{2l+1}\right) + V_I^{lm}(R_{MT^\mu})\left(\frac{r_\mu}{R_{MT^\mu}}\right)^l$$

Where $r_> = max\{r_\mu, r'\}$ and $r_< = min\{r_\mu, r'\}$. Aside from the potential generation from the total charge density, this procedure is also used to gain the correction potential to project out source terms as sketched in 2.2.2. Two things need to be kept in mind when the source density is used with the Poisson equation solver programmed according to [32]:

a) When performing calculations with GGA functionals, the magnetic fields used

for the derivative already have a contribution that stems from a differentiation in real space. The fields are transformed back into the spherical harmonics/plane wave representation, but especially in the MT discontinuities and noise resulting from this will remain in the radial functions. A second and even third differentiation of these functions, as it is done to find the correction to the field, can lead to instabilities and problems with the convergence of the system.

b) By construction, the potential generation requires each radial function corresponding to the angular quantum number l in the density to be at least of order $l-1$ to ensure the integrals for the spherical multipole expansion are finite. A differentiation by r reduces the order of a function by one and the derivatives are scattered to one order above and below when calculating the divergence of the magnetic field and the gradient of the correction potential. This is troublesome, when terms of too low order are scattered to channels with higher l.

2.4.5. The SCF-loop in FLAPW

Regarding the remaining steps of the SCF-loop sketched in 2.1.6, there is one caveat that needs to be addressed in FLAPW. Since the plane wave basis is augmented with radial functions, the plane waves are no longer orthogonal, as the MT-part is cut out off the integration. The contribution from the radial functions is non-orthogonal, as in principle each function couples to all plane waves. Hence, there will be a non-vanishing overlap matrix $S(\boldsymbol{K})$ that needs to be addressed.

$$S^{\boldsymbol{G}'\boldsymbol{G}}(\boldsymbol{K}) = \langle \varphi_{\boldsymbol{G}'}(\boldsymbol{K}) | \varphi_{\boldsymbol{G}}(\boldsymbol{K}) \rangle = \int d^3r \; \varphi^{\star}_{\boldsymbol{G}'}(\boldsymbol{K}, \boldsymbol{r}) \varphi_{\boldsymbol{G}}(\boldsymbol{K}, \boldsymbol{r})$$

This results in a deviation from the simple by the books eigenvalue problem, yielding a generalized eigenvalue problem of the form:

$$(h - \epsilon_\nu S)\boldsymbol{c}_{\boldsymbol{K},\nu} = 0$$

This can, however, be transformed to a regular one by a Cholesky decomposition of the overlap matrix and an appropriate modification of the Hamiltonian and eigenvector. After the resulting problem is solved, the eigenvalues are obtained and the eigenvector can be found by transforming back.
The Fermi energy E_F, i.e. the energy up to which the bands will be occupied, is calculated via Brillouin zone integration. The numerical equivalent to this is a sum

over all occupied bands ν and Bloch vectors $\boldsymbol{K}$ of the integrand multiplied by a set of wave vector dependent weights $w(\boldsymbol{K})$. It is required, that the total number of electrons per unit cell N is conserved in such an integration.

$$N = \sum_{\boldsymbol{K}} \sum_{\nu} w_\nu(\boldsymbol{K})$$

The band dependent weights are defined as the product of the integration weights and the Fermi function with a user defined Fermi smearing parameter $k_B T$:

$$w_\nu(\boldsymbol{K}) = w(\boldsymbol{K}) \frac{1}{e^{(\epsilon_\nu(\boldsymbol{K}) - E_F)/(k_B T)} + 1}$$

The Fermi energy is calculated iteratively by first taking the biggest Eigenvalue from the diagonalization to find the number of occupied bands and from there matching it to the electron number N until the conservation above is fulfilled.

$$N = \sum_{\boldsymbol{K}} \sum_{\nu \leq \nu_{occ}} w_\nu(\boldsymbol{K})$$

All wave functions below the maximal band index will contribute to the new electron density. It is, in general, constructed as:

$$\rho(\boldsymbol{r}) = \sum_{\boldsymbol{K}} \sum_{\nu, \epsilon_\nu(\boldsymbol{K}) \leq E_F} w_\nu(\boldsymbol{K}) |\psi_\nu(\boldsymbol{K}, \boldsymbol{r})|^2$$

There are many more delicate points to consider about constructing the quantities for BZ integration and density generation in each specific region, but those considerations are not the main point of this thesis. The density is mixed with the one from the iteration before to yield the input for next one according to figure 2.1.

3. Testing the modification in elemental magnets

The quality and effects of projecting out magnetic source-terms and scaling the fields need to be tested on materials, whose properties are well-known and in good agreement between experiment and prediction. An obvious choice for such are the elemental ferromagnets. These are body-centric cubic iron (bcc-Fe), face-centered cubic nickel (fcc-Ni) and hexagonal close-packed cobalt (hcp-Co). Those solids need no special tools such as DFT+U or non-collinear magnetism to accurately find and describe their ground state, therefore they are easy to handle and are only treated in a collinear fashion (albeit with spin-orbit coupling enabled). The materials will be tested regarding different questions. In the original paper by Sharma et al. [2], the procedure heavily impacts the magnetic moment per atom calculated with the Elk code [3], reducing it to non-viable values using only the projection. The additional scaling of the input magnetization density and the resulting magnetic field is done to ensure the spin separation is strong enough to converge the densities. Only these two methods used in tandem yielded good results for the elemental magnets and heavily improved results for the more complex materials, that normal SDFT failed to describe accurately. The following sections will each deal with one specific investigation like the overall effect on the energy landscape and the question of the optimal scaling parameter.

3.1. Effect of source-free magnetism on body-centric cubic iron

Since the modification only changes the exchange-correlation magnetic field and leaves the scalar potential unchanged, one would expect that the structure of the solid is not fundamentally changed but only affected to a small extent. To test this assumption, the dependency of the total energy per unit cell in relation to the lattice constant

is tested in body-centric cubic iron. The constant is expressed in relation to the experimental lattice constant of 2.8665 Å and the resulting curve is fitted against the Birch–Murnaghan equation of state (Appendix A) to obtain the minimizing lattice constant. The scaling constants proposed in the original paper are 1.12 for the LDA functional in [33] and 1.14 for the GGA approach of [34]. The following figures show the curve for the unmodified case, the bare source-free modification and the same modification with an additional scaling as proposed by Sharma et al. respectively. Note, that the parametrization of the LDA functional is not the exact same as in Sharma's paper, but rather the one of Perdew and Zunger from [35].

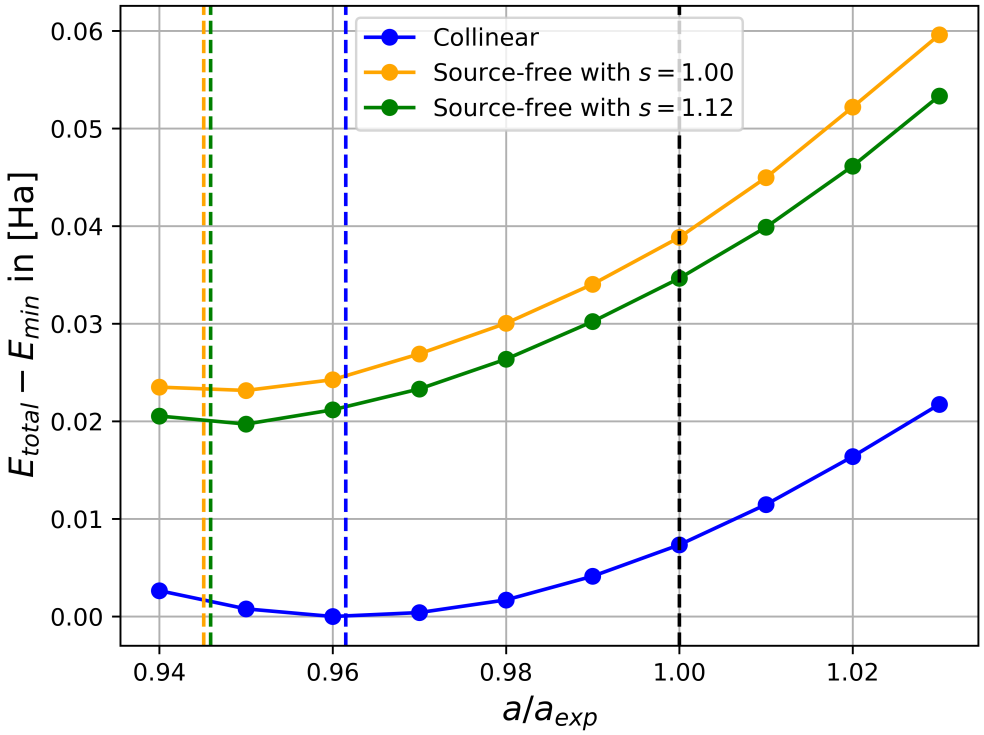

Figure 3.1.: Total energy per unit cell for different lattice parameters in PZ-LDA. The minimal energy value from the collinear calculations E_{min} was subtracted. The black dotted line represents the experimental lattice constant, while the colored ones mark the optimized lattice constants for the data of the same color.

The relevant parameters chosen for the calculations were k_{max} = 3.8, G_{max} = $G_{max,xc}$ = 11.5, l_{max} = 8, $l_{max,nonsph.}$ = 6 and R_{MT} = 2.2 a_0. The k-point grid was initialized with 10 points in each direction, leading to a total of 1000 k-points. The

curves are well behaved with respect to their overall form, with no strong deviations from the collinear case, except for a surprisingly large shift of the minimum for the source-free case. The additional scaling does not shift the minimum significantly further. The GGA curves paint a different picture with higher impact by the scaling:

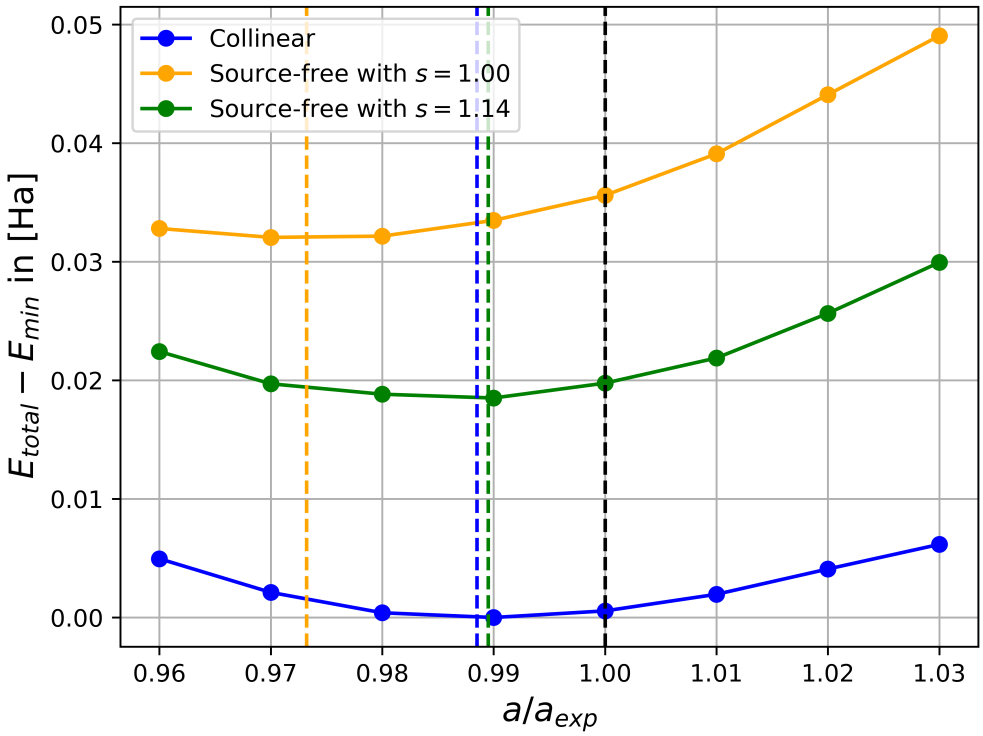

Figure 3.2.: Total energy per unit cell for different lattice parameters in PBE-GGA. The minimal energy value from the collinear calculations E_{min} was subtracted. The black dotted line represents the experimental lattice constant, while the colored ones mark the optimized lattice constants for the data of the same color.

Two things are worth mentioning regarding the qualitative convergence of the ferromagnetic system.

a) The calculation takes at least twice as many iterations to converge when compared to the collinear case. This is expected, as non-collinear magnetism inherently yields more degrees of freedom for the energy landscape to vary in and the modification via the source-term potential drastically changes the magnetic field for every iterative step. Also, the runtime is several times longer, as the Hamiltonian is no longer diagonal in spin-space.

b) The convergence of the GGA functional is much worse than that of the LDA one. The modification tends to amplify deviations of the magnetic moments from high-symmetry directions and shifts the moments away from a pure alignment along the z-axis. This will be discussed in detail when the magnetic moments are analyzed in 3.2. It is known, that (at least for the Fleur code in particular) PBE-GGA is not well-suited to treat non-collinear magnetism, as it was not designed with more than the spin-up and spin-down densities in mind and the handling of the magnetization derivative is ambiguous[4].

Concerning the calculated lattice constant, it is easy to see that the removal of source-terms reduces the optimal cell volume for both functionals, while scaling up the fields leads to an increase. The overall curves for the modified calculations are also shifted upwards. The specific position of the minimum and the shape off the curve are sensitive to the interplay of the contributing energy terms, that of course changes significantly when the magnetism is modified, so it is no surprise that all fitting parameters are changed drastically for the source-free cases. Interestingly, the scaling has a much less pronounced effect in the LDA case. The table below summarizes the fitted parameters from the energy minimization and the resulting magnetic moments. Columns with no subscript in the headers indicate collinear calculations (LDA/GGA), the subscript SF stands for the source-free calculations with no scaling and the subscript s indicates a scaling of 1.12 for LDA and 1.14 for GGA calculations.

	LDA	LDA_{SF}	$LDA_{SF,s}$	GGA	GGA_{SF}	$GGA_{SF,s}$	Exp.
a in Å:	2.76	2.71	2.71	2.83	2.79	2.84	2.87 [36]
B_0 in GPa:	236	251	248	200	235	279	169[37]
B_0':	3.670	2.626	3.565	8.562	1.623	1.000	/
$m_{x,MT}$ in μ_B	0	0	0	0	-0.03	0.01	/
$m_{y,MT}$ in μ_B	0	0	0	0	0.02	0.07	/
$m_{z,MT}$ in μ_B	1.99	1.48	1.81	2.23	1.73	2.16	/
M_{cell}/atom in μ_B	1.97	1.49	1.80	2.23	1.73	2.16	2.20 [38]
M_{Sharma} in μ_B	2.15	1.91	2.22	2.27	1.90	2.16	/

Special care needs to be taken when talking about the definition of the magnetic moment per atom. The mean magnetization for each MT is readily available, while for mono-atomic systems one could also look at the total moment per unit cell divided by the number of atoms. Here, both values are given to see by what margin

[4]As mentioned in the previous footnotes.

they differ. The values are taken at the respective minimizing lattice for each case as highlighted in the previous figures. The additional fitting parameters, the bulk modulus B_0 and its pressure derivative B_0', are also given to quantify the change in shape for the energy curve.
The table shows that the modification has a slight effect on the direction of the magnetic moment in the GGA case. The direction of the magnetic moments deviates from the easy axis, which is a very undesirable effect and is not physically sound, as there is no reason for this symmetry breaking. Since no such effect appears in the LDA calculations, this can only be attributed to the interaction with the derivatives used in GGA calculations. It was already mentioned in 2.4.4 that the repeated execution of derivatives might prove difficult to handle and in the previous footnotes, that a recent change was made to the definition of the gradient used, so this effect is not entirely inexplicable. This will have a far more pronounced impact when talking about antiferromagnetic structures. Interestingly, something similar happened to Sharma et al. when investigating the bulk properties of nickel and cobalt in a follow-up work [39], albeit they applied the [33] LDA functional. They did, however, not take special note of this and did not investigate further.
It is well known, that the lattice constant that LDA calculations yield does not realistically describe the experimental findings for ferromagnetic iron [18] which is reflected in the strong deviation of all calculated moments from the experimental value of $2.20\mu_B$. For the further discussion of the magnetic moments and other investigations, all calculations will be done for the PBE-optimized lattice constant from the collinear case, as it yields data much closer to the experimental value. The resulting moments are summarized here.

Calculation:	LDA	LDA_{SF}	$LDA_{SF,s}$	GGA	GGA_{SF}	$GGA_{SF,s}$
$m_{x,MT}$ in μ_B	0	0	0	0	0.03	-0.05
$m_{y,MT}$ in μ_B	0	0	0	0	-0.03	0.02
$m_{z,MT}$ in μ_B	2.15	1.75	2.12	2.23	1.84	2.19
M_{cell}/atom in μ_B	2.14	1.85	2.08	2.23	1.84	2.18
M_{Sharma} in μ_B	2.15	1.91	2.22	2.27	1.90	2.16

These results are in better agreement with the Elk code used by Sharma et al., though the initial removal of source-terms seems to have a bigger impact overall. The scaling reproduces very similar results in the GGA case, which is the easiest to compare as it uses the exact same functional instead of a similar but different parametrization. The moments averaged over each MT and the total moment per

cell averaged over the atom count are also in sufficiently good agreement to warrant using MT averages to define the notion of the magnetic moment per atom and will be considered for the following tests. This is also important as the cell average will be zero for antiferromagnets hence making the calculation of their moments only possible in the MT by default. In the LDA case, the slight difference in cell and MT moments shows that the interstitial carries a small negative moment. This means all calculations can be slightly dependent on the MT radius, which is why it will be kept as consistent as possible throughout further calculations. As a next step, it is crucial to conserve the defining property of iron - being a ferromagnet - hence finding a higher ground state energy for an anti-parallel alignment of spins in contrast to a parallel one. As an example, the LDA case at the PBE-optimized lattice constant is tested alongside the magnetic moment for the MT:

	LDA	LDA_{SF}	$LDA_{SF,s}$
$E_{tot,FM}$ in Ha	-2541.1504556983	-2541.1205073750	-2541.1243080849
$E_{tot,AFM}$ in Ha	-2541.1242373942	-2541.1228941545	-2541.1210011056
$m_{MT,FM}$ in μ_B	2.15	1.75	2.12
$m_{MT,AFM}$ in μ_B	±1.03	±0.0	±0.60
ΔE in mHa	26.2	-2.39	3.31

It is easy to see, that the source-free treatment acts very differently on ferro- and antiferromagnetic iron. As opposed to the ferromagnetic case, it now leads to a demagnetization for antiparallel spins and the scaling of the fields does not recover the magnetic moments nearly as good as before. The unscaled case even prefers the demagnetized state to the ferromagnetic one, which is not a physical result. The energy difference is heavily influenced and far removed from the initial collinear value. This means antiferromagnetic structures need to be handled with extra care and require a sufficient scaling. It is very likely that this is true for all non-parallel spin structures and may be significant when extending the scope of the treatment to more complex materials. The same test was attempted for the PBE-GGA functional, but the aforementioned general problems with non-collinear usage of GGA made converging the system impossible and the spins stayed only roughly antiparallel, while the magnetic moments did not show the same absolute value, meaning the configuration was not antiferromagnetic anymore.

3.2. Optimal scaling parameters in Fleur

Now that the impact of the scaling on the resulting quantities and fields has been highlighted, it is essential to find an 'optimal' scaling for the Fleur code. This differs from the optimal scaling in the Sharma paper, as they employed the Elk code to compute their results and a different LDA functional is chosen. The main difference is the treatment of magnetism in DFT as a whole. While Elk treats magnetism in 2nd variation as a perturbation after a non-spinpolarized spin basis is found for a first run, Fleur is based on the approach of a spin-polarized basis with up- and down basis functions. The determined scaling was found to be roughly universal across the materials studied in the paper. It is, however, not a physical but rather a computationally motivated variable, that needs to be redetermined for the different framework used in this thesis.

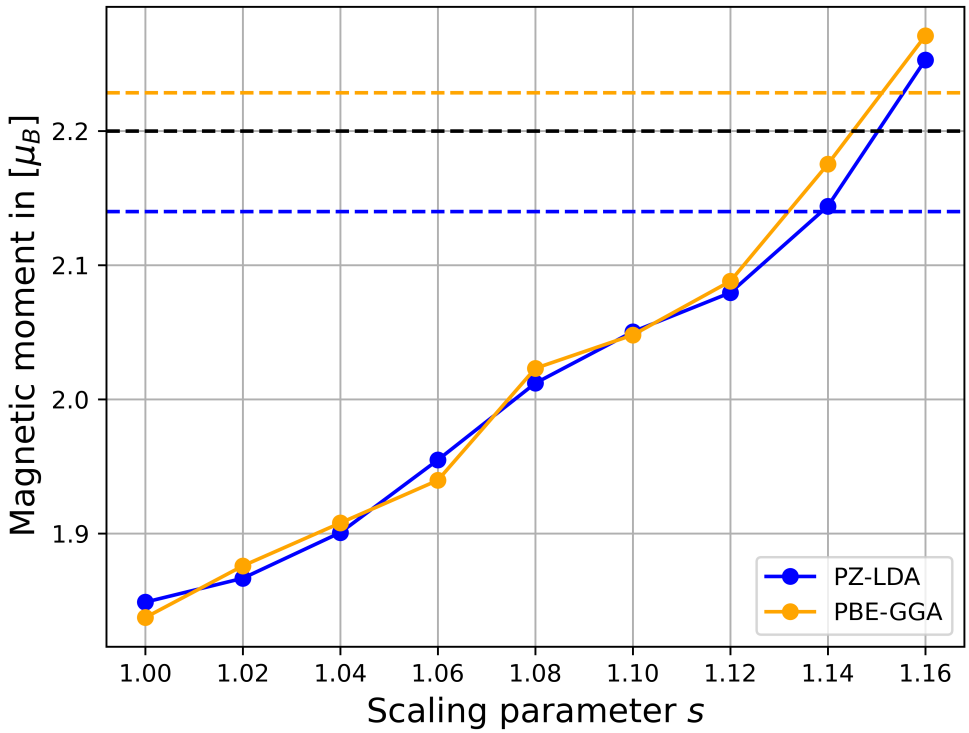

Figure 3.3.: Magnetic moment per iron atom in bcc-Fe for different scaling parameters s. The dotted black line represents the experimental value and the colored ones mark the moments for collinear calculations with PZ-LDA and PBE-GGA respectively.

The term 'optimal' is defined here in the sense, that the scaling for each functional exactly meets the calculated value of the magnetic moment per atom from the unmodified collinear case. While Sharma et al. based the optimization on a fit to the values for bcc-Fe and the more complex $BaFe_2As_2$, this thesis will instead focus on the three elemental magnets, as they are well understood and therefore form a good basis for the extension to more complex materials.
Figure 3.3 shows the scaling dependency for iron with both functionals. The experimental moment, the moment calculated for the collinear LDA and the collinear case are shown as dotted lines. For this system, the optimal scalings can be determined both for finding the exact experimental moment per atom and alternatively by reproducing the calculated moment from the non-modified collinear case in a reasonable range. The curves look remarkably similar, with the exception that the GGA calculations form a lot less smooth curve. The resulting values for the possible scalings are:

Functional:	LDA	GGA
$s_{exp.}$	1.150	1.145
$s_{col.}$	1.139	1.152

The scalings are somewhat similar to those found by fitting the experimental magnetization against the scaling for iron and $BaFe_2As_2$ in the original paper. For the LDA case, they are a bit larger, which can be attributed to the different functional parametrizations. In the GGA case, they are nearly the same. But he convergence was, again, much more difficult to handle in the GGA case. The calculations never quite finished and were stopped, when at least the magnetization and total energy values settled to a non-fluctuating value.
Nickel, on the other hand, is a different matter. While the convergence for iron was significantly worse for the GGA functional when compared to LDA, it is hardly given at all in the case of nickel. The moments fluctuate wildly with increasing s and no optimal scaling can be determined, because the magnetic moments, that are supposed to be ferromagnetically aligned and therefore of the same magnitude and direction, vary significantly. Albeit a general upward trend can be observed with increasing s just like for bcc-Fe. Due to this lack of convergence with GGA, only the LDA scaling curve is shown and evaluated. The results are shown in figure 3.4:

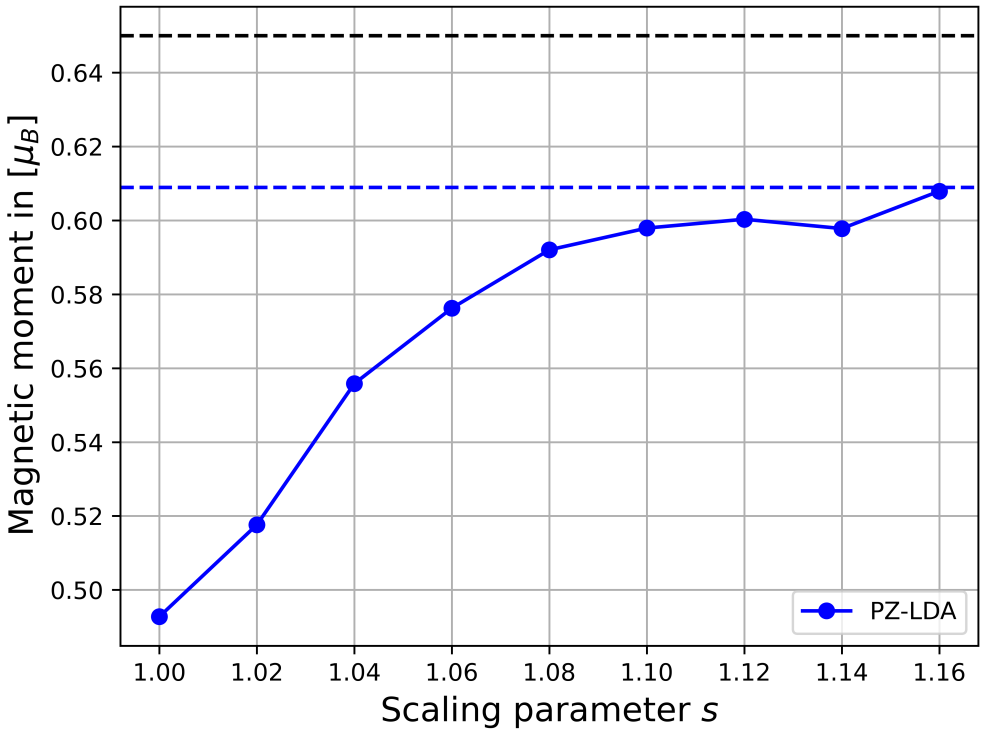

Figure 3.4.: Magnetic moment per nickel atom in fcc-Ni for different scaling parameters s. The dotted black line represents the experimental value and the blue one marks the moment for a collinear calculation with PZ-LDA.

This becomes even worse in cobalt, where the more complex hcp structure prohibits convergence entirely for GGA calculations. Here, not even an overall positive trend for the relation moment vs. scaling can be found, as the magnetic moments first get smaller and then rise again in what resembles a parabola. So figure 3.5 again only shows the LDA scaling curve, which is reasonably smooth and stems from converged calculations.

In both the fcc and hcp cases, the experimental value is not reached before the curve flattens, implying that much higher factors would be needed to find the exact value. This further incentivizes defining the optimal scaling with respect to the value from the collinear case. The resulting values are summed up below and can be averaged with the one from bcc iron to find the mean optimal scaling between the three.

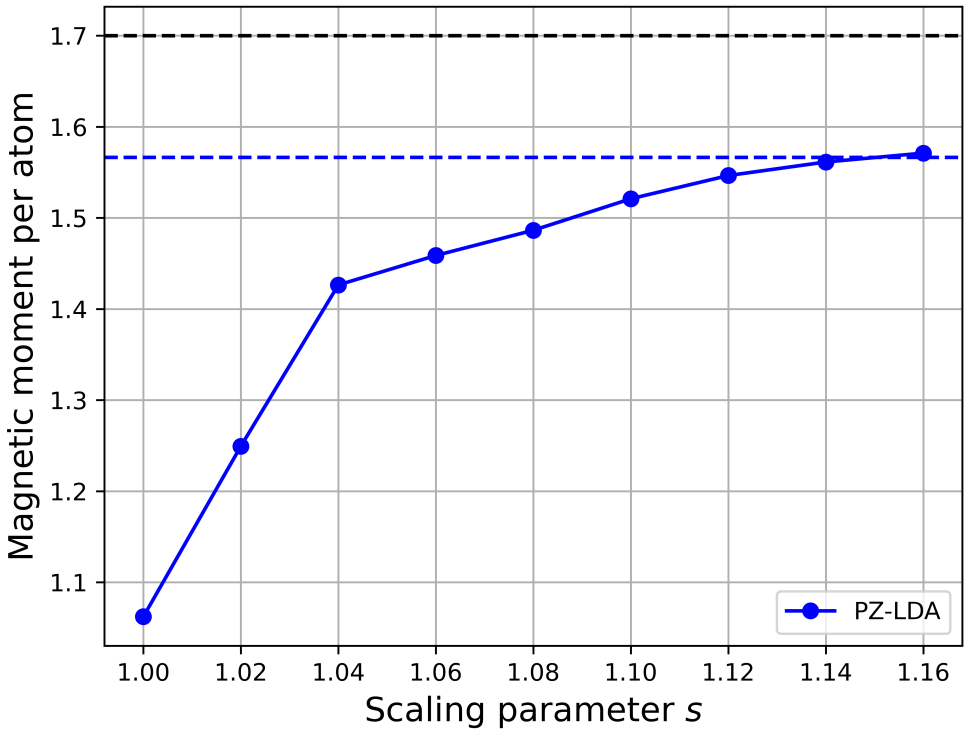

Figure 3.5.: Magnetic moment per cobalt atom in hcp-Co for different scaling parameters s. The dotted black line represents the experimental value and the blue one marks the moment for a collinear calculation with PZ-LDA.

Scaling	Value
s_{Fe}	1.139
s_{Ni}	1.160
s_{Co}	1.151
s_{avg}	1.150

By a simple average of the three distinct values, the resulting optimal scaling is roughly 1.15. This differs from the one found in [2], which is not surprising considering the functional parametrization used is not identical and the reference systems are different. An optimal scaling for GGA calculations can not be determined, so for the rest of this thesis all source-free calculations will be done for the LDA functional.

3.3. Improved Antiferromagnets and Discussion

With the optimal scaling determined for three ferromagnetic structures, the question arises whether the factor is also suitable to describe source-free antiferromagnets. An earlier investigation showed, that a scaling of s = 1.12 was not sufficient to accurately describe antiparallel spins in bcc iron and with no scaling the system tended towards demagnetization. The table below shows as before, the corresponding total energies and magnetic moments but for the optimal scaling of s = 1.15.

Calculation:	LDA	$LDA_{SF,1.15}$
$E_{tot,FM}$ in Ha	-2541.1504556983	-2541.1263266865
$E_{tot,AFM}$ in Ha	-2541.1242373942	-2541.1181114581
$m_{MT,FM}$ in μ_B	2.15	2.16
$m_{MT,AFM}$ in μ_B	±1.03	±0.86
ΔE in mHa	26.2	8.22

The magnetic moments of the antiferromagnetic case are reproduced a lot better for the higher scaling. There is still a reduction, but it is less pronounced and an even higher scaling would likely remedy this.
To summarize the core results of the testing on elementary magnets, the following points will be used as a guideline for achieving the best results:

a) The most realistic lattice constants and magnetic moments are found for an energy minimization with the PBE-GGA functional.

b) The actual calculations for source-free magnetic fields need to be done with the PZ-LDA functional, as the use of PBE-GGA with this form of non-collinear magnetism is highly unstable and the calculations do not converge smoothly or at all depending on the complexity of the system [5].

c) The optimal scaling constant for the fields, as proposed by Sharma et al., in this case is roughly 1.15. This value is able to approximately reproduce the magnetic properties of the elemental ferromagnets in the source-free case.

d) Antiferromagnets are not described very well with LDA functionals, but as the PBE-GGA breaks down completely for source-free antiferromagnets, this is the only option to use. Non-parallel spin structures will have to be handled with special care.

[5] This might very well be cured with the change mentioned in footnotes 2 and 3 on page 10

4. Source-free iron pnictides

In the original paper, the source-free modification of the exchange-correlation magnetic field showed particular success as a means for the description of iron oxypnictides of rare earth metals and iron pnictides of alkaline earth metals. These are materials formed from metallic cations and anions containing elements from group V of the periodic table, the nitrogen family. Materials from this class have risen in interest in recent years for their exotic qualities with respect to magnetism and superconductivity. For example, LaFeAsO was shown to exhibit both long-range antiferromagnetic ordering and superconductivity when doped with hydrogen [10] or flourine [11] in the oxygen sites or with cobalt in the iron sites[40], depending on the temperature, external pressure [12] and doping concentration. As Sharma et al. pointed out, the description of the electronic structure of these materials in a DFT framework was far from accurate, producing values for the magnetic moment on the iron atoms that were up to 275% too big in [2]. This of course is symptomatic for a completely inaccurate representation of the system in the context of its more exotic properties. In the Elk code, they used the source-free treatment to great success, reducing the root-mean-square percentage error (RMSPE) across all the materials they studied to 6% for source-free LDA and 11% for source-free PBE-GGA, albeit with an additional DFT+U treatment for two of the materials. This chapter will deal with the analysis of LaFeAsO and CeFeAsO, two materials with symmetry according to the Cmme space group, and $CaFe_2As_2$, $SrFe_2As_2$ and $BaFe_2As_2$ from the Fmmm space group as examples for the effect of the source-free fields on rare earth oxyarsenides and alkaline earthe diarsenides respectively.

4.1. Pnictides from the Cmme space group

At low temperatures, XFeAsO crystallizes in an orthorombic lattice with a basis according to space group 67 (Cmme). X represents the lanthanide in the pnictide. The unit cell contains 16 atoms and looks as follows for lanthanum:

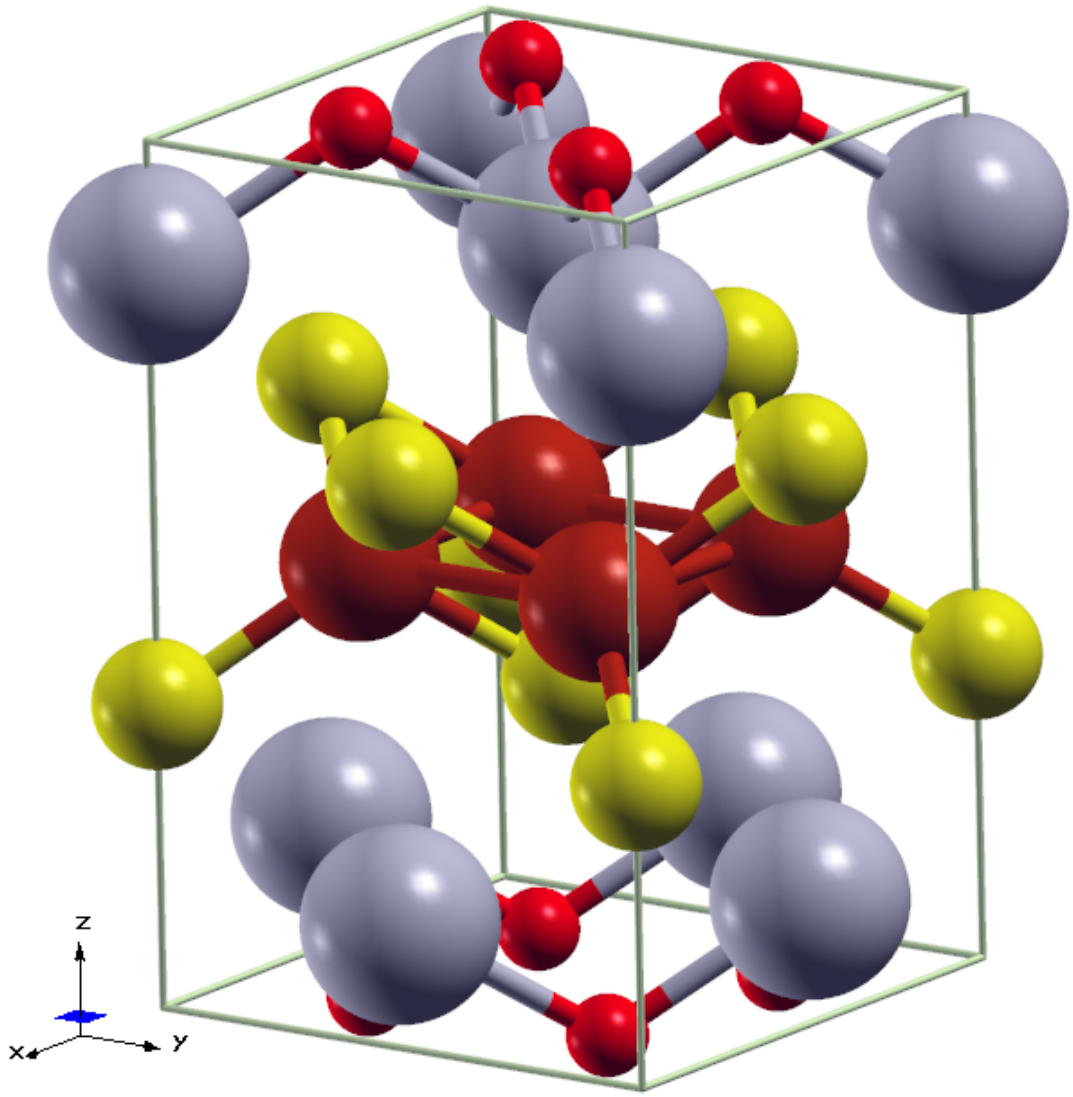

Figure 4.1.: Unit cell of LaFeAsO (Cmme) plotted in XCrySDen [41]. The grey spheres represent lanthanum atoms, dark red is iron, yellow is arsenic and bright red is oxygen.

It forms a layered structure with oxygen atoms embedded in a lanthanum bilayer interchanging with an identical setup of iron atoms embedded in arsenic. The iron atoms in this material are shown to exhibit ferromagnetic order in the shortest axis (x) and antiferromagnetic order in the other two [42]. That means to accurately describe the internal magnetism, a magnetic unit of doubled size in z-direction with 32 atoms is needed. The lattice parameters and atom positions (in internal coordinates) for the single cell are taken from experiments done at 4 K in [40]:

Lattice parameters	
a in Å	5.6823
b in Å	5.7103
c in Å	8.7117
Wyckoff representatives	
La at 4g	(0,1/4,0.1424)
Fe at 4b	(1/4,0,1/2)
As at 4g	(0,1/4,0.6501)
O at 4a	(1/4,0,0)

Each representative is paired with a partner shifted by 1/2 in the y-direction and a negative sign in the z-direction. Additionally, for each of them there is another partner shifted by $(1/2, 1/2, 0)$. Using these values, a first run of test calculations was done with the following parameters: k_{max} = 3.0, G_{max} = $G_{max,xc}$ = 9.0, l_{max} = 10, $l_{max,nonsph.}$ = 8 for lanthanum, l_{max} = 8, $l_{max,nonsph.}$ = 6 for iron and arsenic and l_{max} = 6, $l_{max,nonsph.}$ = 4 for oxygen. The respective R_{MT} are 2.78, 2.20, 2.21 and 1.57 a_0. The k-point grid was set to a low value of $4 \times 4 \times 2$ to quickly check the trends of the calculated magnetizations. For all calculations, a universal smearing of 0.027 eV was applied. All calculations were done with spin-orbit interaction taken into account. The y-aligned antiferromagnetism proposed in several papers was also used to start a separate calculation for comparison.

	LDA	LDA+SF$_{1.12}$	LDA+SF$_{1.15}$	Exp.[43]
$m_{MT,Sharma}$ in μ_B	1.60	0.73	/	0.63
$m_{MT,z-AFM}$ in μ_B	1.17	0.54	0.72	/
$m_{MT,y-AFM}$ in μ_B	0.95	/	1.57	/

At first glance, the magnetic moments trend toward the right direction. The initial moment is corrected downwards in the source-free case and reproduces the experimental one a good deal better. The moments for pz-optimized scaling in Fleur and PW92-optimized scaling in Elk are highly similar. Interestingly, the initial moments without the modification are a tad closer to the experimental value when calculated in Fleur as compared to the Elk code. Using the proposed in-plane antiferromagnetism also improves the result, while the modification makes the prediction worse for this setup. The impact of this simple rotation will be further studied in section 4.3. For the best possible comparison to the known results, the z-aligned case will be studied further with the optimized scaling from this thesis. This is also encouraged by comparing the total energies per unit cell for the different orientations.

	LDA	$LDA_{SF,1.15}$
$E_{tot,z}$ in Ha	-96757.7695474055	-96757.7477071383
$E_{tot,y}$ in Ha	-96757.7646900703	-96757.7423870604
ΔE in mHa	4.86	5.32

The comparison shows, that the z-oriented case is energetically slightly preferable for this exact setup, which of course may be very dependent on the optimized lattice parameters in each direction, but the comparison to the Elk code results is the most sensible with the same z-orientation, so it is be used here as well. Before running more calculations, first the k-point set is made finer to check whether the resulting values are converged or still change. The new sets are $6 \times 6 \times 3$ and $8 \times 8 \times 4$ points.

	LDA	LDA+SF$_{1.15}$
$m_{MT,4\times4\times2}$ in μ_B	1.17	0.72
$m_{MT,6\times6\times3}$ in μ_B	1.19	0.71
$m_{MT,8\times8\times4}$ in μ_B	1.16	0.72

While the values fluctuate a little, which can be due to the complexity of the system, the differences are not very large. The chosen k-point set therefore is big enough for a qualitative comparison of some more similar materials to verify the quality of the modification and another enlargement is not warranted.
There are several other pnictides with the same unit cell structure but with a different lanthanide as its basis, in the following case CeFeAsO. It shows a similar antiferromagnetic pattern for the iron atoms in the longer planar direction but ferromagnetic order with respect to the other two axes. Additionally, the cerium atoms carry their own magnetic moment and also order accordingly, though in an orthogonal instead of antiferromagnetic fashion [44], forming an intricate pattern for the magnetism. Different sources, however, propose different low temperature structures. The paper from which the lattice parameters are taken [44] notes moments flipping their y-component with respect to moving in the x-direction, while a newer paper [45] from which the reference value of m_{Fe} is taken reports x-flips in the x-directions and additional y-flips in y, while the iron atoms align orthogonally to them instead of pointing in the x-direction. The calculations for the rest of this chapter are done for the k-point set of $6 \times 6 \times 3$, moments initially aligned in the z-direction and a scaling of s = 1.15 for source-free Fleur calculations. The MT radius for cerium is again 2.78 a_0 and the Wyckoff z-coordinates are z_{Ce} = 0.1402 and z_{As} = 0.6553 for a unit cell with lattice parameters a = 5.66263 Å, b = 5.63273 Å and c = 8.64446 Å

at $T = 1.4\ K$ [44]. Due to the added magnetism from the cerium atoms coupling to that of the iron, the internal magnetic structure becomes more complicated and the convergence of the ground state density is slower and more sensitive than in the case of non-magnetic lanthanum. The results from [2] do not mention a magnetic moment for cerium, but only for the nearest-neighbour compounds with praseodymium and neodymium (which were then treated with an additional U parameter to account for the strong correlation) so the moment cannot be compared to their findings[6].

	LDA	LDA+SF	Exp.
$m_{MT,Sharma}$ in μ_B	1.64	0.81	0.8 [45]
$m_{MT,Fe}$ in μ_B	1.26	0.93	/
$m_{MT,Ce}$ in μ_B	0.07	0.20	/

It is worth noting, that for the base case the cerium moments are heavily suppressed and only start to emerge with the source-free modification. They align antiferromagnetically along the x-axis, changing directions along the y-axis, while the iron moments align along the z-axis and interchange in x-direction. This picture is different from those found in both reference papers. The magnitudes of the iron moment and its improvement by the modification is very similar to the lanthanum case, in that the unmodified prediction is a bit better than in the Elk case, while the modification brings Elk closer to the experimental value here (if the referenced value from [2] is used). To verify the notion that this trend persists across more materials, the next section will deal with a different class of pnictides.

[6]The citations in the original paper are somewhat off here. The experimental value in the paper Sharma et al. cite is not 0.8 - a value of 0.81 is found in the paper from which they reference the experimental structure data.

4.2. Pnictides from the Fmmm space group

While the first to cases of pnictides were lanthanide iron oxypnictides, containing an equal amount of each constituent per unit cell, Sharma et al. also considered a closely related class of materials formed from alkaline earth metals and twice the amount of iron and arsenic per unit cell. These diarsenides also exhibit the same form of long range antiferromagnetic order in the iron sublattice for the two longer crystal axes, but crystallize in a slightly different structure according to the 69th space group (Fmmm). The main constituent metals show no magnetism, due to their lack of unpaired electrons, and the complete magnetic order is contained within the chemical unit cell (4.2) for low temperatures.

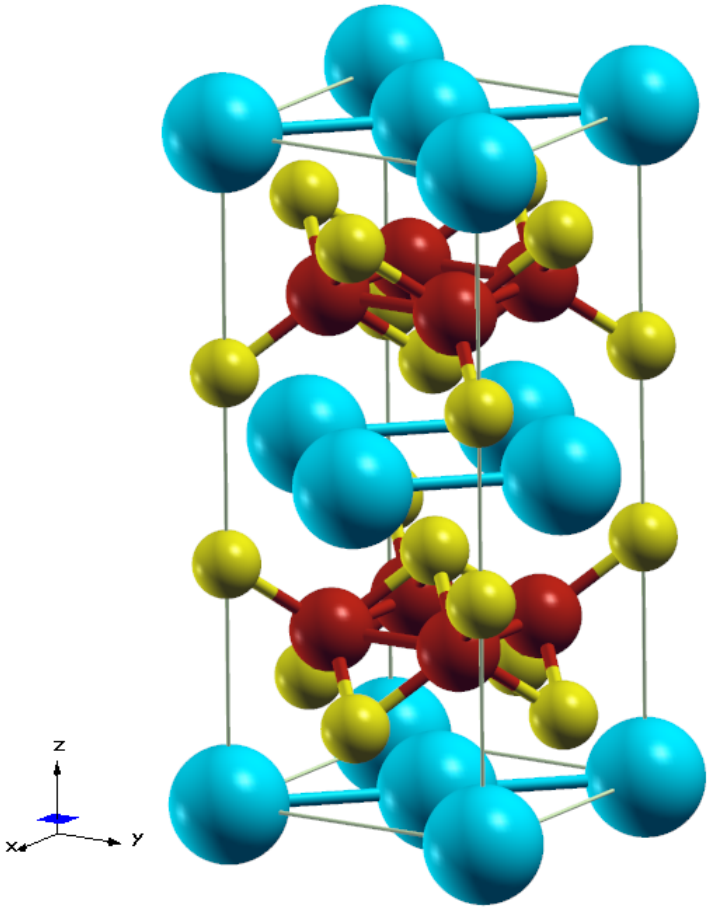

Figure 4.2.: Unit cell of Fmmm structures like $BaFe_2As_2$ plotted in XCrySDen[41]. The blue spheres represent the alkaline earth atoms, dark red is iron and yellow is arsenic.

This means the three materials in question, containing calcium, strontium and barium respectively, are largely similar in structure and properties. The unit cell looks similar to the lanthanide case, but this time with two layers per cell of iron nested in arsenic. The structure in question has a slightly increased atom count of 20 per unit cell as opposed to the 16 that fit into the rare earth pnictides' cmme cell. The structural data used to describe the unit cell is summarized below for AE=Ca[46], Sr[47], Ba[48].

Lattice parameters	AE=Ca	AE=Sr	AE=Ba
a in Å	5.5312	5.5783	5.5447
b in Å	5.4576	5.5175	5.5773
c in Å	11.683	12.297	12.852
z_{As}	0.3689	0.3612	0.3575
T in K	50	90	33
Wyckoff representatives			
AE at 4a	(0,0,0)		
Fe at 8f	$(\frac{1}{4},\frac{1}{4},\frac{1}{4})$		
As at 8i	$(0,0,z_{As})$		

The 8f and 8i coordinates have partners with the same coordinates negated and the resulting five atoms each have partners at $(0, 1/2, 1/2)$, $+(1/2, 0, 1/2)$ and $+(1/2, 1/2, 0)$ for a total of twenty per unit cell. However, caution needs to be taken when comparing these structures to the ones from the previous section. The calculations were done according to the parameter choices from the section before with the additional parameters of $R_{MT,AE}$ = 2.8 and the $l_{max,AE}$ the same as for lanthanum and cerium. The temperatures for which the alkaline earth compounds were examined are significantly higher than for the rare earth pnictides and the usage of the same smearing parameter (that directly relates to the temperature) as it was done in [2] is not necessarily sensible.
Considering that only the iron atoms are magnetic and are therefore the only relevant part for the cells internal magnetic structure, the convergence was smoother than in the case of the doubled unit cell of LaFeAsO or the magnetic cerium interaction in CeFeAsO. The results, compared to the ones from Sharma et al. and experimental findings ([49],[50],[51]) are as follows:

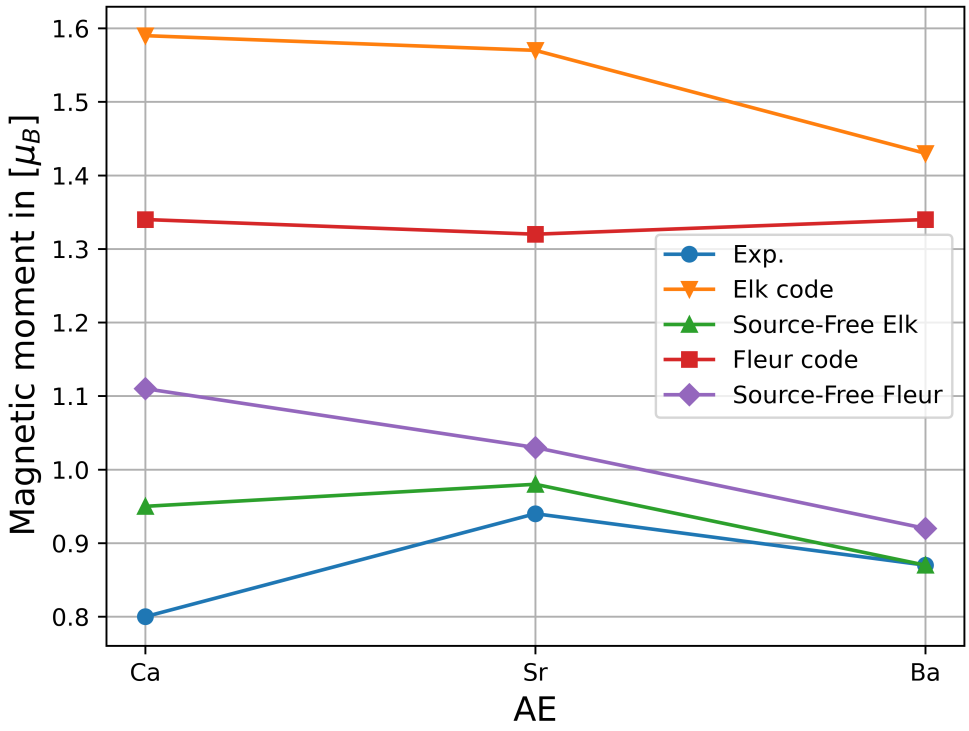

Figure 4.3.: Magnetic moment per iron atom in alkaline earth pnictides.

Several things can be noted here. For one, the initial prediction of the magnetic moments within the Fleur code is a bit lower, matching the very low pnictide moments better than in the Elk case but still being more than a third too big. Second, the source-free modification reduces the moments in both cases so they are far closer to the experimental values, with the agreement getting better with increasing atomic number in both frameworks. Third, the matching of the barium moment is perfect as computed with the Elk code. This is due to the fact, that $BaFe_2As_2$ was chosen alongside iron to find the optimal scaling parameter that was then used for all calculations. As this thesis opted to instead base the scaling on all three elemental magnets as the most unbiased basis, the agreement is of course not as great. Considering this last fact, the improvement can be seen as in good agreement with the results from [2] and the general notion, that the initial description is a bit better in Fleur, is reinforced. This can be best seen when looking at all calculated moments with respect to their percentage deviation from the experimental value.

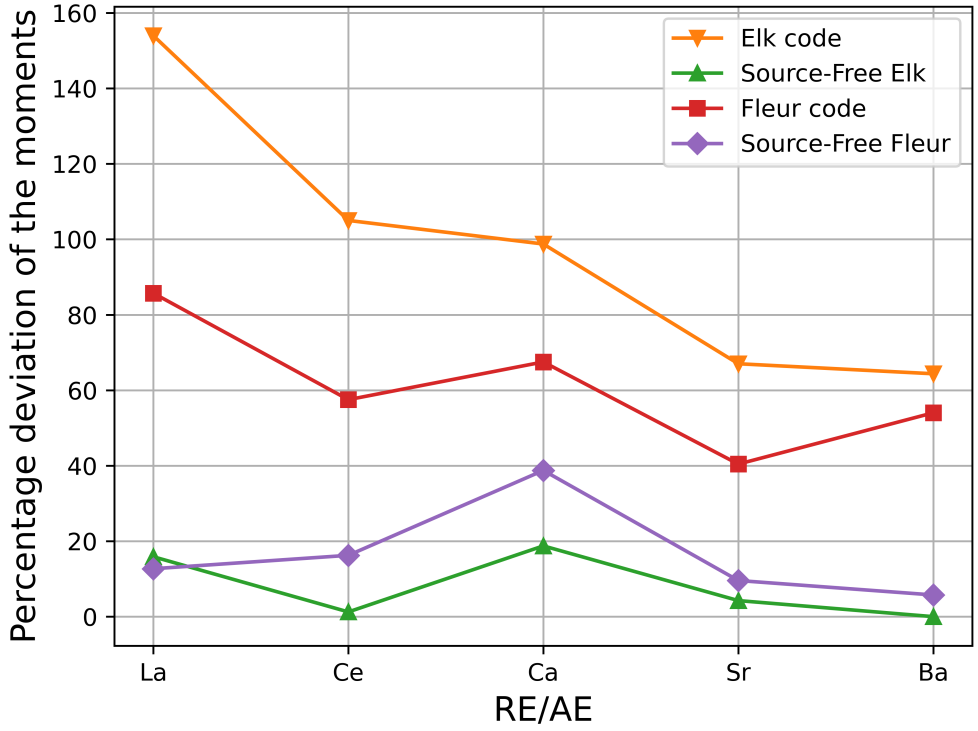

Figure 4.4.: Percentage deviations of iron magnetic moments in rare earth/alkaline earth pnictides.

Except for the case of LaFeAsO, where the magnetic moments in both codes become roughly equal in the source-free variant, the aforementioned trend is obvious. Another point to note is that the level of improvement is vastly different across the different materials. LaFeAsO and $CaFe_2As_2$ are improved to around the same deviation while $CaFe_2As_2$ started with a better initial description to begin with. This also differs between the two frameworks. The calcium moment shows the worst improvement across the five materials studied, but the percentile deviation is only half as big when computed with Elk. These and several other points highlighted so far will be discussed in the final section of this chapter.

4.3. Lattice optimization of $CaFe_2As_2$

In chapter 4.1 it was noted, that the calculations in [2] yielded magnetic moments aligned along the z-axis rather than the antiferromagnetism along the x-axis found for the low temperature phases of most of the pnictide superconductors. In the same chapter, an improved magnetic moment could also be found for LaFeAsO by adhering to this proposed order and without the application of the source-free modification. The following short section serves as a check, how much of an improvement can be gained this way combined with a thorough lattice optimization in both the lattice parameters and the relative height of the referential arsenic layer z_{As} of $CaFe_2As_2$. As this material was described worst by the source-free modification and is the most manageable in terms of its internal magnetism and electron count, the calculation is made easier than for the other four. The parameters were kept mostly the same in comparison to the last section, but the k-point set was refined to $16 \times 16 \times 8$ and, as it is more suitable for structure optimizations, the functional used was PBE. First, the general direction in which an optimization is needed the most is analyzed:

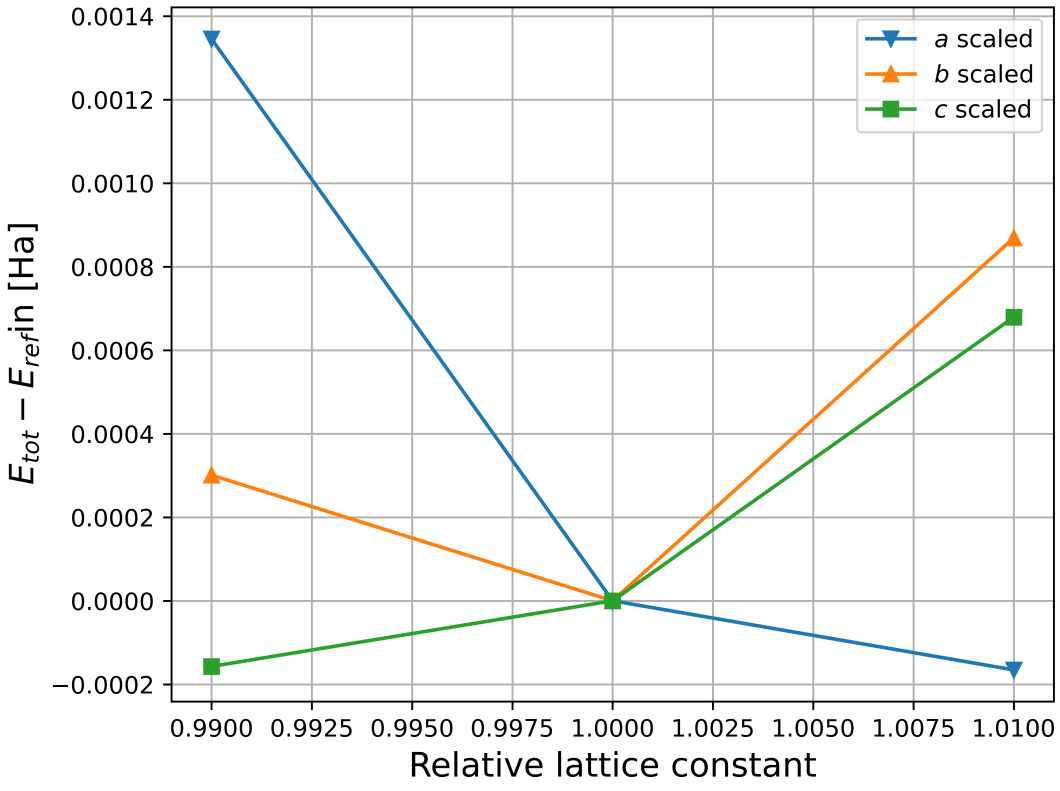

Figure 4.5.: Energy landscape in $CaFe_2As_2$ for the different lattice parameters.

According to this figure, an optimization in lattice parameter a is most significant due to the steepness of the curve, c is the next most significant and (under the assumption of non-interference between the three) an optimization in b will not yield much change, since the minimum is already somewhat well met at the experimental value. Therefore the structure optimizations will be done in the order: $a \rightarrow c \rightarrow z_{As}$. Figure 4.6 shows the optimization with respect to a:

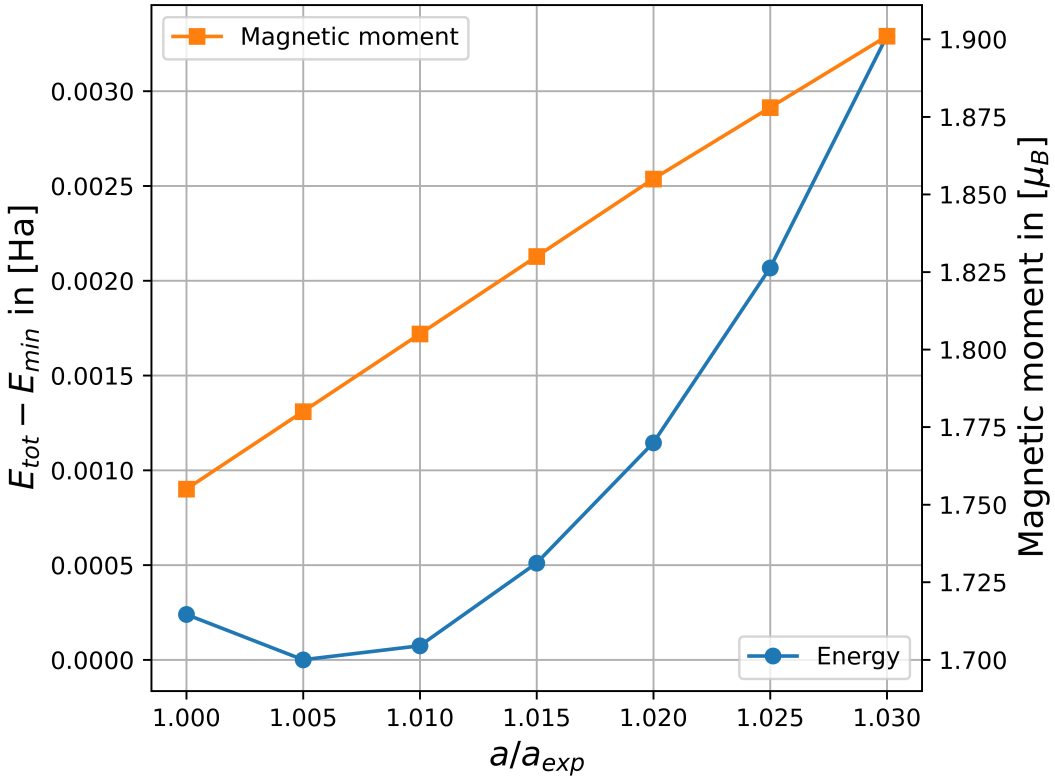

Figure 4.6.: Energy landscape and magnetic moments of $CaFe_2As_2$ with respect to the lattice parameter a. The blue energy curve adheres to the scale on the left side of the figure and the magnetization values are found on the right.

The energy curve shows a distinct minimum. The magnetic moments increase with growing separation, as can be expected of the antiferromagnetic structure embedded in the lattice. Interestingly, the increase shows a very distinct linear trend. The optimized value is roughly a = 5.558 Å and gives a magnetization value of $1.79\mu_B$. Next, the minimization in c (figure 4.7) is added. The optimized parameter a is already taken into account.

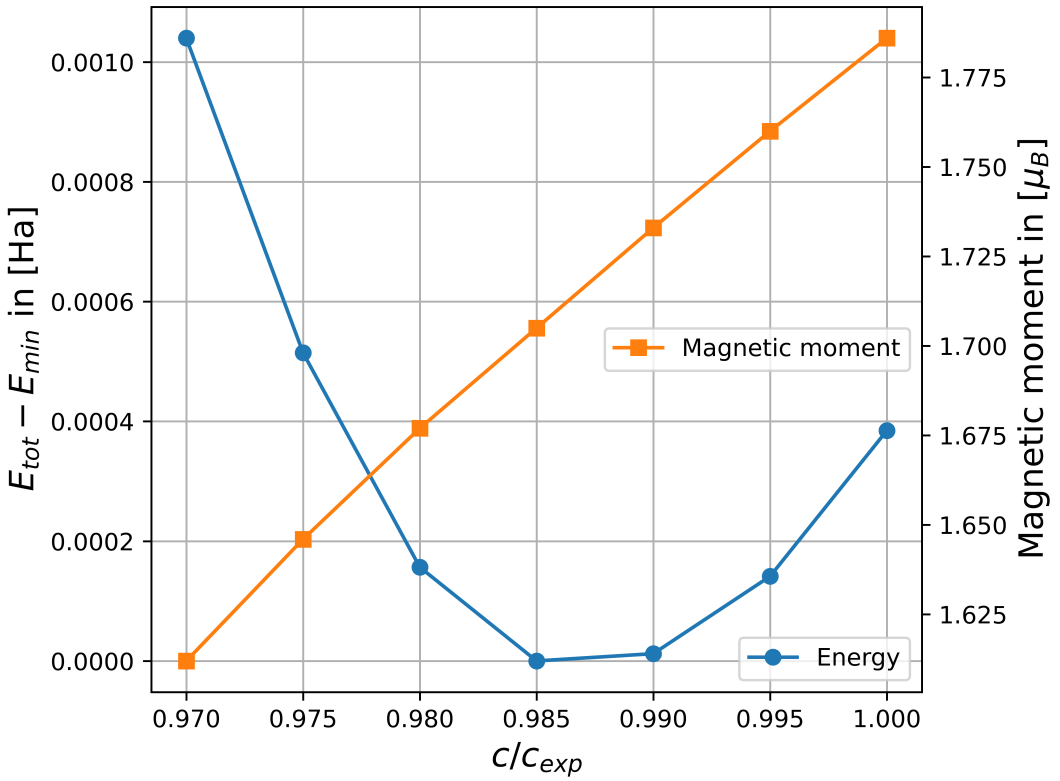

Figure 4.7.: Energy landscape and magnetic moments of $CaFe_2As_2$ with respect to the lattice parameter c. The blue energy curve adheres to the scale on the left side of the figure and the magnetization values are found on the right.

As there are two antiferromagnetically aligned layers of iron atoms in the $CaFe_2As_2$ unit cell, the reduction of the magnetic moment with decreasing distance is again quite natural. A linear trend is again visible, although with a significantly lower slope. This is most likely due to the overall increased distance between the iron atoms in c direction and the atom layers between them. The optimized lattice parameter is c = 11.538 Å. The last optimization is done with both optimized lattice parameters fixed.

Figure 4.8 shows the last curve and highlights the sensitive dependence of the magnetic moment per iron atom on the interatomic spacing inside the cell. While the moment varied by $< 0.2\ \mu_B$ for expansions and compressions of one spatial direction by up to 3%, the 1% changes in the layer position vary it by around 0.35 μ_B. So while the magnetic moment is very sensitive to all three optimizations, the last one has the

most profound impact. The optimized height for the representative arsenic atom is around $z_{As} = 0.3675$.

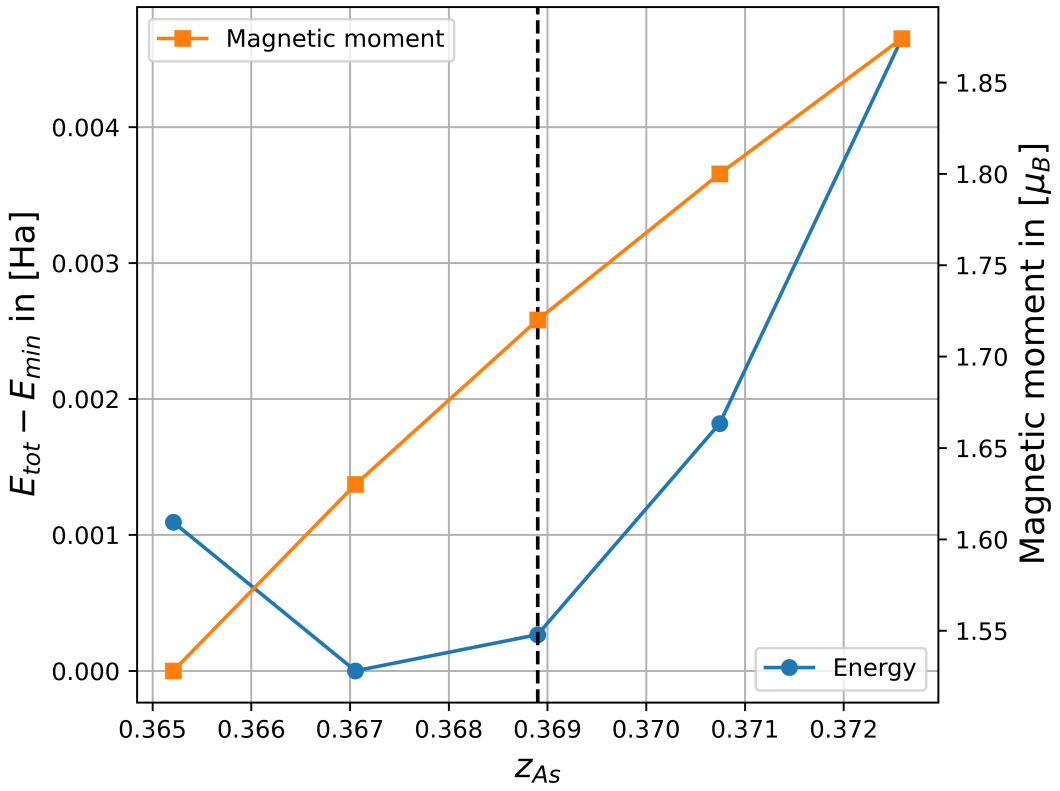

Figure 4.8.: Energy landscape and magnetic moments of $CaFe_2As_2$ with respect to the position of the representative arsenic layer z_{As}. The blue energy curve adheres to the scale on the left side of the figure and the magnetization values are found on the right.

The results of the minimization with respect to the calculated magnetic moment are found in the table below. All moments are given in multiples of μ_B and m_0 refers to the non-optimized calculations done for the experimental lattice parameters.

m_{exp}	0.8
m_{Sharma}	1.86
m_0	1.76
$m_{a\ opt.}$	1.79
$m_{c\ opt.}$	1.72
$m_{z\ opt.}$	1.65

There are two key observations here. The moment is sensible to structural changes but ultimately not much different too the reference case, as the experimental lattice constants and the PBE-optimized ones are very close. Also, the expansion in a and compression in c compete in changing the moment up- and downwards. Also, the calculated moment agrees well with the one found in [2] for the unoptimized case. This means, that taking the x-alignment into account did not lead to a major change in the description of the complex magnetism in $CaFe_2As_2$.

4.4. Discussion

In [2], Sharma et al. proposed the manual removal of source terms from the magnetic field motivated by theorems from CDFT that state the equivalence of varying the magnetic moment and its curl for certain properties. They identified the problems in the description of pnictide magnetism as stemming from unphysical source terms in the exchange-correlation magnetic field. The previous sections showed, that the removal of these terms does indeed improve the calculated moments, but that is not necessarily saying the assumption is verified. The procedure was shown to affect ferromagnetic and antiferromagnetic structures very differently in the sense, that the ferromagnetic moments for the elemental magnets are closely reproduced for an appropriate scaling, while the same scaling reduces the magnetic moment per atom for an antiferromagnet to a significant degree. This can directly be observed for the pnictide materials, which are all exhibiting antiferromagnetic ordering of the iron atoms in the x-y-plane, as the predicted moments for each of them is reduced and none are enlarged. So it stands to reason, that the improvement is somewhat constructed and not a natural consequence of adhering to the laws restricting physical magnetic fields.

Another matter is the overall structure of the pnictides. Experimentalists showed that for each of the materials in question an antiferromagnetic ordering occurs along the short in plane axis (also pointing in the same direction), baring exceptions like the complex ordering in CeFeAsO and the additional antiferromagnetic ordering in the z-axis of LaFeAsO. A visualization of the magnetic fields in [2] clearly shows, that the magnetic moments point perpendicular to the iron layers, while the alignment is in agreement with the experiments. This means the ground state structure differs, making deviations of the magnetic moments between experiment and the DFT result more likely. It was shown, that for LaFeAsO the magnetic moment could already be improved by a significant amount by considering the experimentalists ordering (4.1), but a further investigation of this effect for $CaFe_2As_2$ showed that this was not a universal trend. This is also not the only factor that needs to be taken into account. Earlier DFT investigations of the high temperature phase of LaFeAsO also relied on a description with an additional U parameter [52] as did calculations done for doped pnictides [53].

As a last short remark, the overall better quality of the unmodified Fleur calculations as opposed to Elk can be justified with one of the central differences between the

structure of the two codes. Fleur relies on an explicit treatment of magnetism through a spin-polarized basis set, while Elk uses a second variation scheme founded on a non-spin-polarized one. The latter treatment inherently assumes that magnetic effects can be treated as a rather small perturbation. In the case of complex magnetism between four to eight iron atoms per unit cell, it becomes increasingly questionable to speak of such a small perturbation and it is sensible, that the somewhat more elaborate spin-polarized basis yields better results.

5. Magnetic ordering and coupling in source-free iron

Initial investigations in chapter 3.1 showed that the source-free modification and the scaling of the magnetization density and magnetic field had a noticeable impact on the lattice constant of the ferromagnetic iron crystal. The impact was more pronounced for the PBE-GGA functional, that proved difficult with respect to the removal of source terms and was not used for further calculations, but was also present in the PZ-LDA structure. Furthermore, antiferromagnetic bcc iron was also inspected to find that the energy difference between the FM and AFM state was significantly altered when source terms were removed and the antiferromagnetic moments were highly reduced instead of roughly conserved like for the ferromagnet. In the light of these findings, the following chapter will further investigate the ground state properties of elemental iron structures. It is a well tested result, that the local density approximation predicts iron should crystallize in a fcc ground state structure (γ-iron), which is a state found in experiments only for heated iron, and not in the well documented bcc structure (α-iron). This holds true for the implementation in the Fleur code as well. It will be shown, whether or not the impact of the modification as significant enough to change this fact. Additionally, the alteration of the magnetic coupling constants in a Heisenberg model will be examined closer.

5.1. The Source-Free iron ground state

The first two structures under consideration are the most basic (anti-)ferromagnetic ones iron can form, the bcc and fcc crystals. That means in the first case, one atom is inserted into the middle of a simple cubic structure and in the second case one sits in the middle of each face. Since the atomic radius of iron does not change for the different structures, the fcc one is necessarily larger and the unit cell needs to be set up accordingly. To adjust for this fact, the reference lattice constant for bcc iron is

taken to be the experimental value of 2.8665 Å and the one for fcc is scaled up by a factor of $\sqrt{3/2}$ according to considerations done for a hard sphere model of both structures. In both cases, the antiferromagnetic structure was taken to be one with layered ordering, meaning the atoms located at $z = 1/2$ were initialised with opposite spin to the ones at $z = 0$ and $z = 1$. The calculations were all done for the same set of initial parameters to gain maximal comparability. Most notably the choice was $R_{MT} = 2.15$, $k_{max} = 4.0$, $G_{max} = G_{max,XC} = 12.0$, $l_{max} = 8$, $l_{max,nonsph.} = 6$, $s = 1.15$ and a k-point set of $16 \times 16 \times 16$. The ferromagnetic calculations were started for an initial moment of $2\mu_B$ and the antiferromagnetic ones with $\pm 1.5\mu_B$ per iron atom. The results for the bcc structures are shown in figure 5.1.

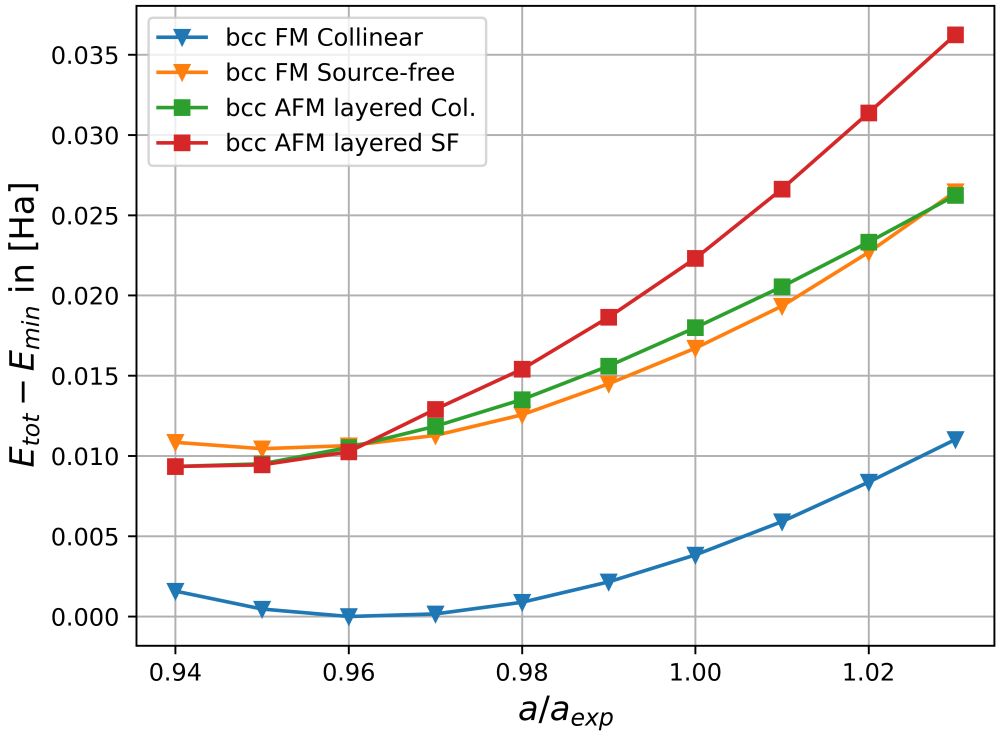

Figure 5.1.: Total energy per atom in bcc-Fe for source-free and collinear magnetism as a function of the lattice constant.

As noted before, the modification raises the overall energy level for both ferromagnets and antiferromagnets. The antiferromagnetic calculations, however, yield small lattice constants. They also converge to the exact same value, implying that the source-free ground state is equal to the unmodified one. This can only happen for

vanishing magnetism. To verify this notion, the average magnetization per muffin tin is plotted against the lattice scaling as well.

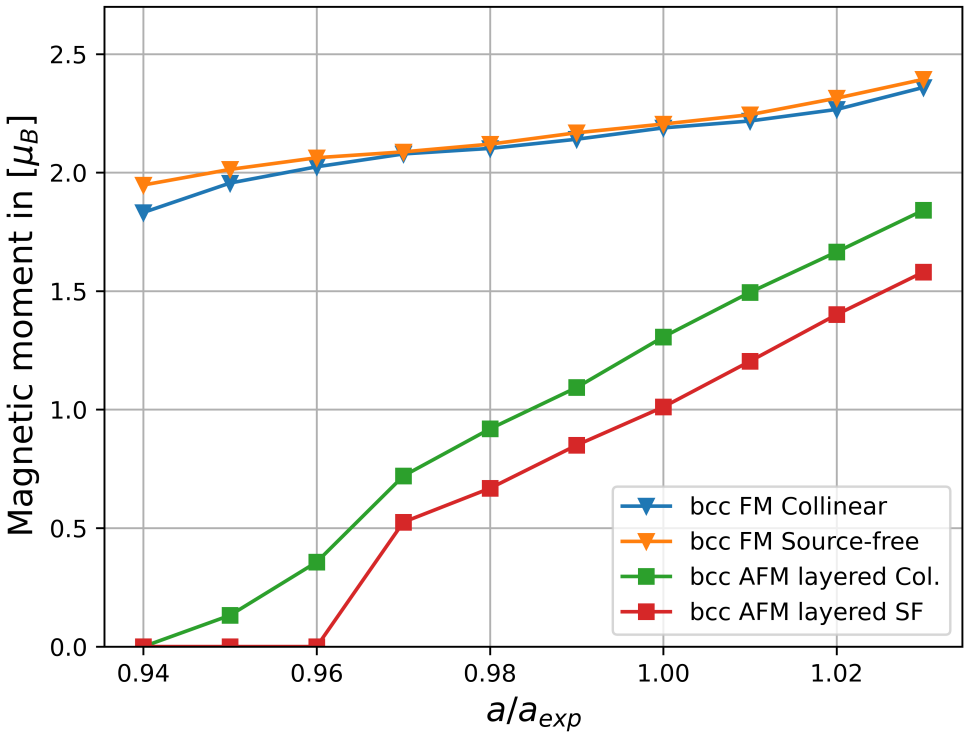

Figure 5.2.: Magnetic moment per atom in bcc-Fe for source-free and collinear magnetism as a function of the lattice constant.

Several properties need to be highlighted here. First, the magnetic moments for the ferromagnetic case are highly similar between the collinear reference calculation and the source-free modification. Especially around the PBE-optimized lattice constant, this is obvious by construction, since the scaling s constant was fixed to achieve this effect. It is notable, however, that the overall curve is very similar in its entirety. For the antiferromagnet, the figure shows that a compressed lattice leads to a demagnetization of the system and an actual antiferromagnetic order only arises from a certain minimal lattice constant upwards. It then increases approximately linear in strength with the lattice constant for both the modified and unmodified system, with the source-free magnetism having overall smaller moments. This is in agreement with earlier findings, that the optimal scaling for ferromagnets does not perfectly recover antiferromagnets as well but rather still weakens them for the optimal scaling. This is

also reflected in the onset of antiferromagnetism being shifted towards higher lattice constants, meaning the lattice needs to be stretched further to allow the order to set in. With the investigation of the actual magnetic order found for the different calculations, the picture of the energy landscape changes.

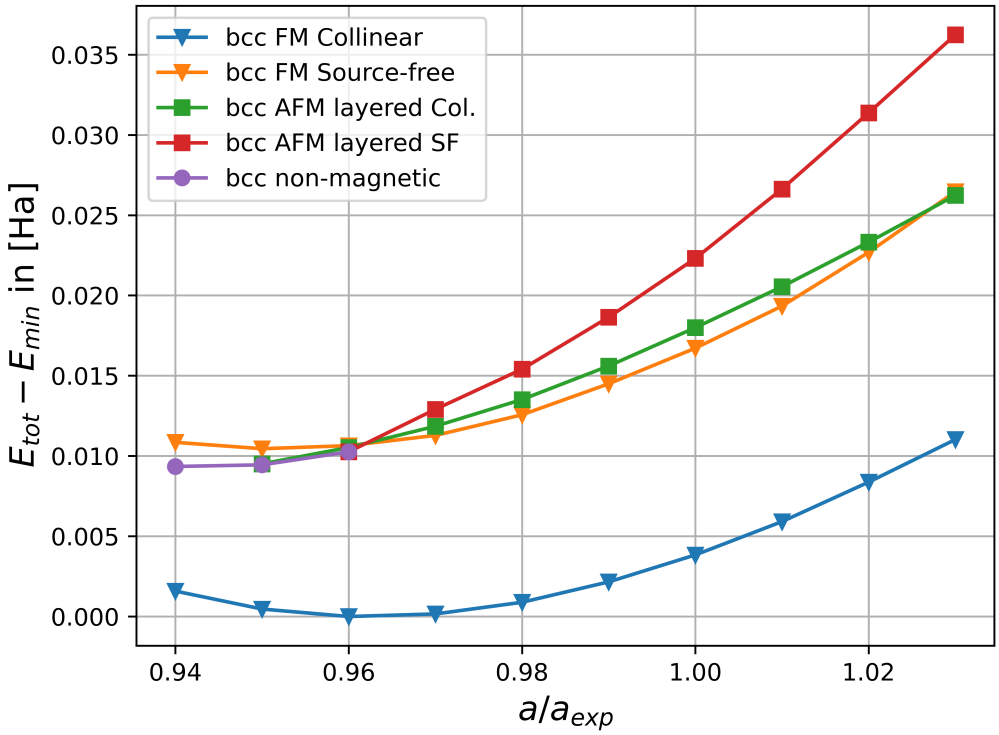

Figure 5.3.: Refined total energy per atom in bcc-Fe for source-free and collinear magnetism or non-magnetized states.

This means, that in the unmodified case, bcc iron will crystallize as a ferromagnet with a lattice constant of around 2.76 Å, while the source-free structure favors a non-magnetic state with a lowered lattice constant. The minimal distance between the iron atoms with upward and downward polarization that makes antiferromagnetism possible (and coincides with the nearest-neighbour distance) is calculated to be roughly 2.358 Å for a normal collinear antiferromagnet and 2.480 Å for the source-free structure.

The same investigation is done for fcc iron with a scaled up reference lattice constant of 3.5107 Å. No other parameter was changed and the initial results are shown in figure 5.4. The curves for different starting conditions all converge towards lower

lattice constants and identical energy values, implying that again the system tends to be non-magnetic for a compressed lattice and this time even the ferromagnetic phase can only form for high enough distances between the iron atoms. I.e. the energy minima for all curves coincide and a non-magnetic state with a lattice constant of around 3.38 Å is assumed.

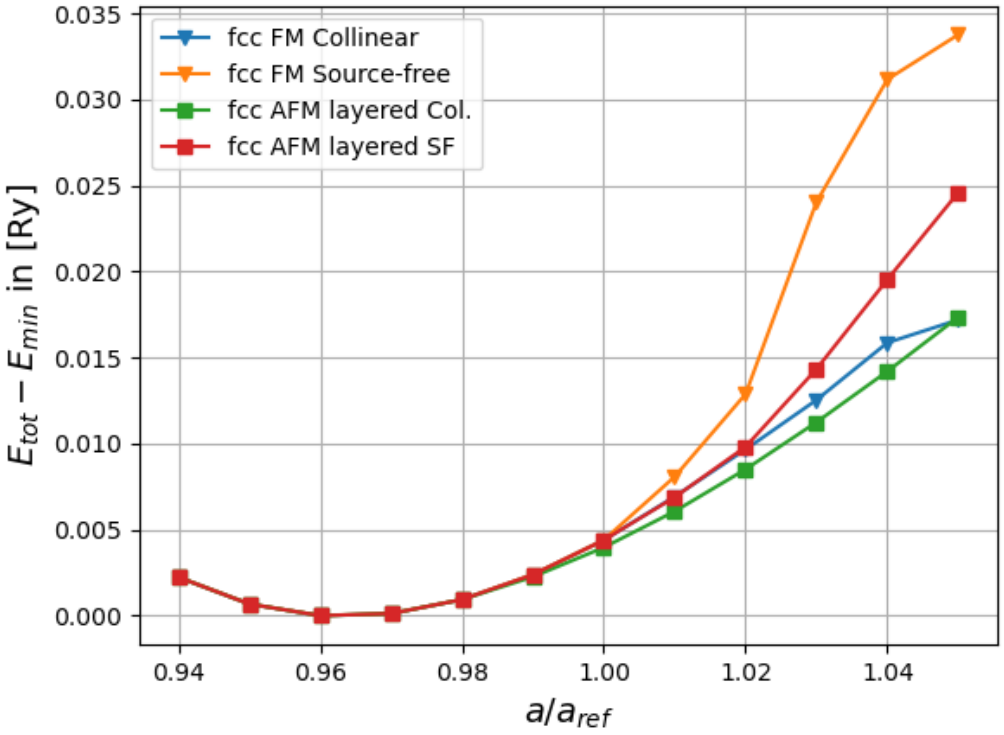

Figure 5.4.: Total energy per atom in fcc-Fe for source-free and collinear magnetism/non-magnetism as a function of the lattice constant.

Figure 5.5 shows the behaviour of the magnetic moments in the fcc case. It is again validated, that the smallest lattices show no magnetism at all. Interestingly, the relation between the unmodified collinear and source-free case is vastly different from the bcc structure. While a minimal lattice constant is needed again to magnetize the system, the ferromagnetic phases are much less similar than before and for an expanded lattice the source-free moment is greatly enlarged when compared to the standard calculation for intermediate lattice constants. For bigger lattice expansions they appear to reconverge. This means, that the similarity between the conventional and source-free moments found before is exclusive to the bcc structure and, more

generally, there is no simple relation between the collinear and modified moments. The harsh reduction of antiferromagnetic moments in again visible nonetheless.

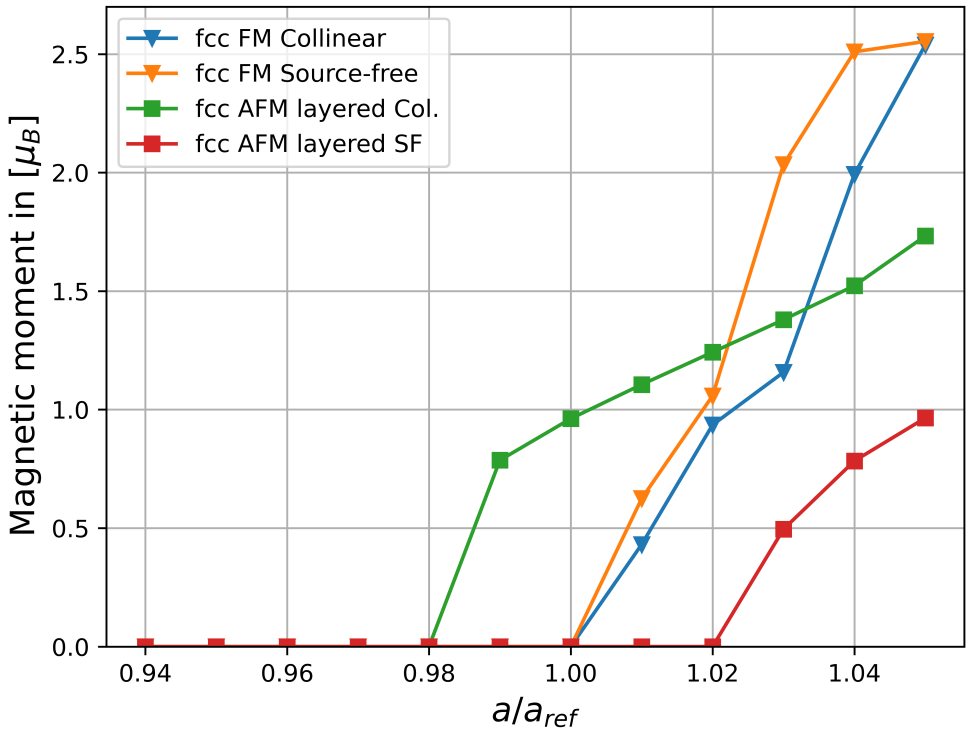

Figure 5.5.: Magnetic moment per atom in fcc-Fe for source-free and collinear magnetism.

The shift of a_{min} is also a lot more pronounced here than in the case of bcc iron for the antiferromagnet and the moment is reduced even more significantly. The minimum distance for the collinear antiferromagnet is around 2.4550 Å, the modification increases this to 2.5542 Å. The ferromagnetic state will form for a distance greater than 2.5406 Å. From this an important observation can be made. The removal of source-terms and its impact on the magnetic order of a system is not only dependent on whether a ferro- or antiferromagnet is examined, but also on the arrangement and distance of the magnetic atoms within the lattice. The overall trend that can be seen is, that the modification disfavors magnetism as a whole and in both investigated cases reduces the resulting moments for antiferromagnetic structures. This information will be crucial in understanding, why the modification works the way it does. In short, it can be noted that the source-free antiferromagnetism is suppressed while the

ferromagnetism is (especially for the bcc structure) closer to its original strength and this might very well be the effect responsible for improving the description of pnictides, as their iron atoms are antiferromagnetically aligned and all their calculated moments are too high initially.

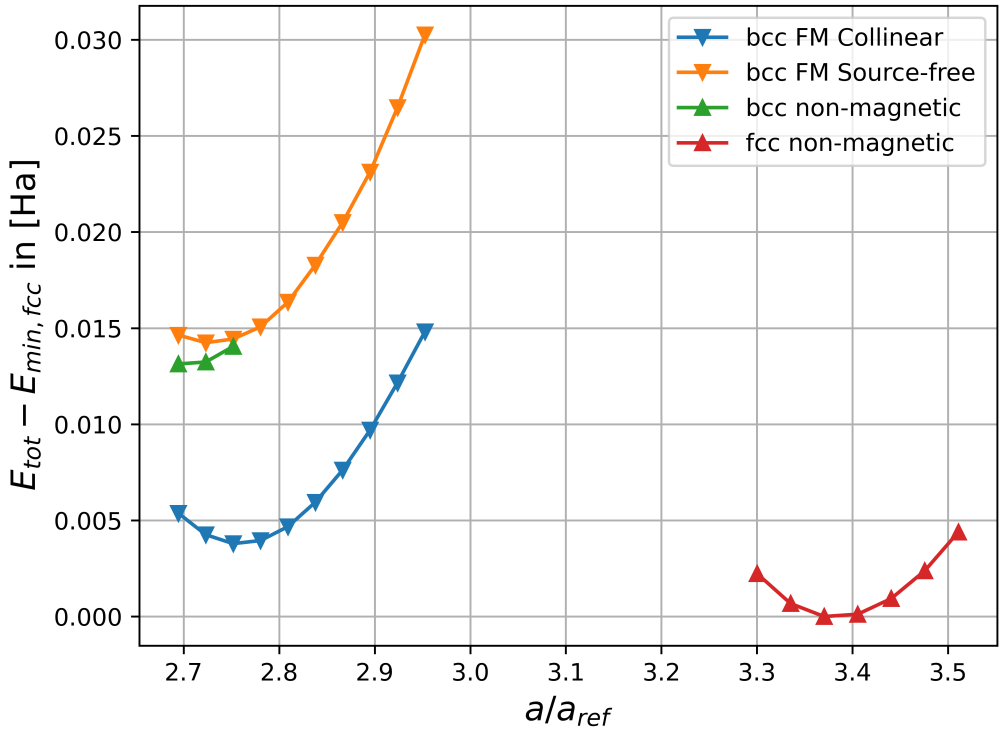

Figure 5.6.: Energy landscape for optimized bcc/fcc iron structures with and without source terms.

As a conclusion to this section, figure 5.6 shows the complete energy landscape for the different optimized iron structures. The fact that LSDA DFT predicts iron to assume a non-magnetic fcc ground state is not changed by the removal of magnetic source-terms. Considering the fact, that the modification is not supposed to affect non-magnetic states this is not all too surprising. The impact on the exact moments and optimal order on the other hand is profound in antiferromagnets and ferromagnetic fcc structures. For the bcc structure the already too low ferromagnetic lattice constant is further reduced and a non-magnetic state is predicted to be slightly favorable. This speaks against the validity of the modification, as it would be desirable to not worsen the calculated properties of simple materials with respect to experimental

results only to improve the description of more exotic ones. This would be akin to fixing the U parameter of a DFT+U calculation such that it perfectly reproduces experimental findings. The exact impact on the ordering behaviour in iron structures will be further analyzed in the following section, with respect to the coupling parameters governing the interaction in a generalized Heisenberg model.

5.2. Coupling parameters from different magnetic iron structures

To quantify the claim, that projecting out the source fields influences the way an iron structure will order, this section deals with the calculation of coupling parameters in a Heisenberg model from the total energies of different (anti-)ferromagnetic iron crystals. This is not by all means an accurate model for the complex magnetism as treated in DFT by FLAPW, as magnetism in the interstitial region is explicitly allowed and contributes to its overall magnetic moment, but for this purpose it will suffice. The focus will be on bcc and fcc type structures in a layered magnetic order. In the Heisenberg model, the magnetic ordering will then be governed by the number of atoms per unit cell and the number of neighbours with the same and opposite spin that they have. This simplifies the formulae in chapter 2.3 to:

$$E_{cell} = E_0 - J_1 S^2 \sum_i \sigma_i (N^{\uparrow}_{n.n.} - N^{\downarrow}_{n.n.}) - J_2 S^2 \sum_i \sigma_i (N^{\uparrow}_{n.-n.n.} - N^{\downarrow}_{n.-n.n.})$$

Where i counts the atoms in the unit cell and $\sigma_i = \pm 1$ depending on whether atom i has a positive or negative moment. The numbers N_x denote how many nearest/next-nearest positive/negative neighbours atom i has. To calculate the couplings $J_{1/2}$, one needs three differently aligned structures of the same size. For the bcc case, the setup consists of five layers of iron atoms (three of which constitute a standard bcc structure with two atoms per unit cell like in the previous section) with a total of four iron atoms needed to uniquely describe the structure. This essentially means doubling the stochiometric unit cell (in z-direction) and setting up a tetragonal structure. Measured with respect to the bcc lattice constant a_{bcc}, the structure is summarized in 5.2. The three structures that will be set up are a ferromagnetic one, with all moments aligned along the z-axis, an antiferromagnetic structure with alternating layers of positively and negatively aligned moments (similar to the iron antiferromagnets from sections 3.3 and 5.1, but with double the length in z-direction) and an antiferromagnetic structure with alternating double layers of ferromagnetically aligned moments. Considering that every atom in the unit cell directly corresponds to a layer in these systems, one can associate the ferromagnetic system with an ordering of $\sigma_{1,2,3,4} = (\uparrow, \uparrow, \uparrow, \uparrow)$ [referred to as FM], the single-layered antiferromagnet with $\sigma_{1,2,3,4} = (\uparrow, \downarrow, \uparrow, \downarrow)$ [AFM1] and the double-layered antiferromagnet with $\sigma_{1,2,3,4} = (\uparrow, \uparrow, \downarrow, \downarrow)$ [AFM2]. The structures will be referred to by this notation in the following.

a	a_{bcc}
c	$2a_{bcc}$
$\boldsymbol{r}_{Fe,1}$	$(0,0,0)$
$\boldsymbol{r}_{Fe,2}$	$(1/2,1/2,1/4)$
$\boldsymbol{r}_{Fe,3}$	$(0,0,1/2)$
$\boldsymbol{r}_{Fe,4}$	$(1/2,1/2,3/4)$
$d_{n.n.}$	$\sqrt{3}a_{bcc}/2$
$d_{n.-n.n.}$	a_{bcc}

This makes the calculation of the coupling parameters from the energy rather simple. In general an atom in a bcc lattice has 8 nearest neighbours, which can be found in the next layers up and down the z-axis, and 6 next-nearest neighbours, one in each direction of the encompassing simple cubic structure. For the FM structure, all atoms are equivalent, their moments align with the z-axis and they therefore have 8/6 spin-up neighbours. This means the sums over all neighbours reduce to:

$$E_{cell,bccFM} = E_0 - 32J_1S^2 - 24J_2S^2$$

It does not become much more complicated for the antiferromagnets. For AFM1 each atom has 8 antiferromagnetically aligned nearest and 6 ferromagnetically aligned next-nearest neighbours. In AFM2 each atom has an equal amount of 4 parallel and antiparallel neighbours with 4 parallel and 2 antiparallel next-nearest neighbours. The resulting formulae are shown below.

$$E_{cell,bccAFM1} = E_0 + 32J_1S^2 - 24J_2S^2$$

$$E_{cell,bccAFM2} = E_0 - 8J_2S^2$$

The calculation parameters are the same for all three cases: $R_{MT} = 2.2$, $k_{max} = 4.0$, $G_{max} = G_{max,XC} = 12.0$, $l_{max} = 8$, $l_{max,nonsph.} = 6$, $s = 1.15$ and a k-point set of $16\times16\times8$ k-points (reduced from the previous section to account for the doubled size in the z-direction). The ferromagnetic calculation was started with an initial moment of $2.2\mu_B$ and the antiferromagnets with $\pm1.5\mu_B$. Figure 5.7 shows the results for the coupling constants as calculated from the formulae above for different lattice constants and therefore nearest neighbour distances. Only configurations that converged into an (anti-)ferromagnetic ground state were considered, while those that demagnetized were sorted out.

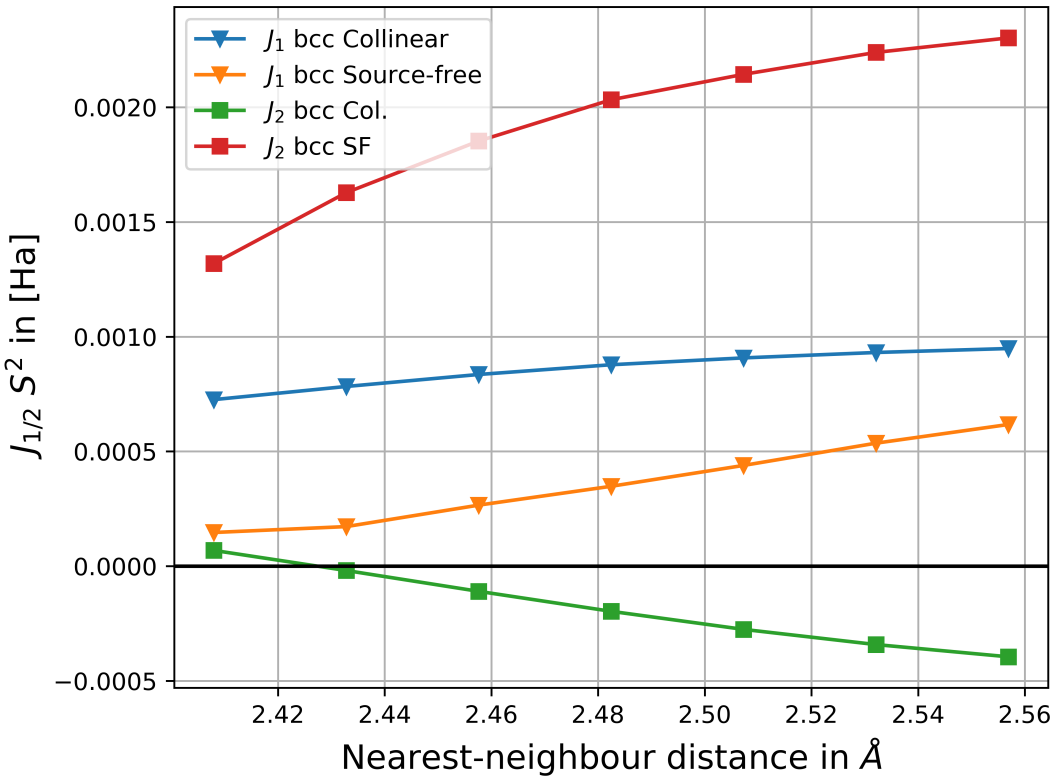

Figure 5.7.: First and second order Heisenberg coupling parameters for bcc iron structures depending on the nearest-neighbour distance.

The plot shows the heavy impact of the source-free modification on the coupling constants and therefore on the ordering behaviour of the iron structure. While in the unmodified case $J_1 > 0$ and (mostly) $J_2 < 0$, in principle allowing both ferro- and antiferromagnetism for appropriately large distances, the source-free case has only positive couplings, prohibiting the formation of antiferromagnets in a system governed by only the Heisenberg interaction and strongly suppressing it for ab initio DFT calculations. This is reflected in the increased minimum distance between the atoms that allows antiferromagnetic order and in the reduced magnetic moments. To exclude the possibility that this is an effect related specifically to the bcc structure of the magnet, the same calculations were done for an fcc structure with an increased lattice constant like in the previous section. The structural considerations are very much the same as for the bcc layers, setting up two fcc cells on top of each other to enable the creation of three distinct magnetic structures. These are again a pure ferromagnet (FM), a single-layered antiferromagnet (AFM1) and a double-layered

antiferromagnet (AFM2). Only this time, due to the increased amount of atoms per unit cell, pairs of two of them correspond to the same layer and therefore the same magnetic alignment.

a	a_{fcc}
c	$2a_{fcc}$
$\boldsymbol{r}_{Fe,1}$	$(0,0,0)$
$\boldsymbol{r}_{Fe,2}$	$(1/2,1/2,0)$
$\boldsymbol{r}_{Fe,3}$	$(1/2,0,1/4)$
$\boldsymbol{r}_{Fe,4}$	$(0,1/2,1/4)$
$\boldsymbol{r}_{Fe,5}$	$(0,0,1/2)$
$\boldsymbol{r}_{Fe,6}$	$(1/2,1/2,1/2)$
$\boldsymbol{r}_{Fe,7}$	$(1/2,0,3/4)$
$\boldsymbol{r}_{Fe,8}$	$(0,1/2,3/4)$
$d_{n.n.}$	$a_{fcc}/\sqrt{2}$
$d_{n.-n.n.}$	a_{fcc}

Each atom now has 12 nearest and still 6 next-nearest neighbours. Of the nearest neighbours, 4 lie in the same plane as the respective atom, so they are always parallel, and 4 atoms each lie in the next layer up- and downwards. For the ferromagnet this of course still yields only positive contributions to the summations in the energy calculation and gives:

$$E_{cell,fccFM} = E_0 - 96J_1S^2 - 48J_2S^2$$

For the single-layered antiferromagnet, there are always 4 neighbours with the same alignment from its own plane and 8 opposite ones from the neighbouring planes. All next-nearest neighbours share the alignment of the respective atom. This amounts to:

$$E_{cell,fccAFM1} = E_0 + 32J_1S^2 - 48J_2S^2$$

In the double-layered structure there are 8 parallel and 4 antiparallel neighbours in contrast, due to one neighbouring layer being aligned in the same direction. The next-nearest neighbours from the same plane are again parallel, but those 2 planes across are necessarily antiparallel. This leads to:

$$E_{cell,fccAFM2} = E_0 - 32J_1S^2 - 16J_2S^2$$

The formulae are not much different from the bcc case and the calculation of the couplings is therefore just as easy. The results for the varying lattice constant are

shown in the figure below:

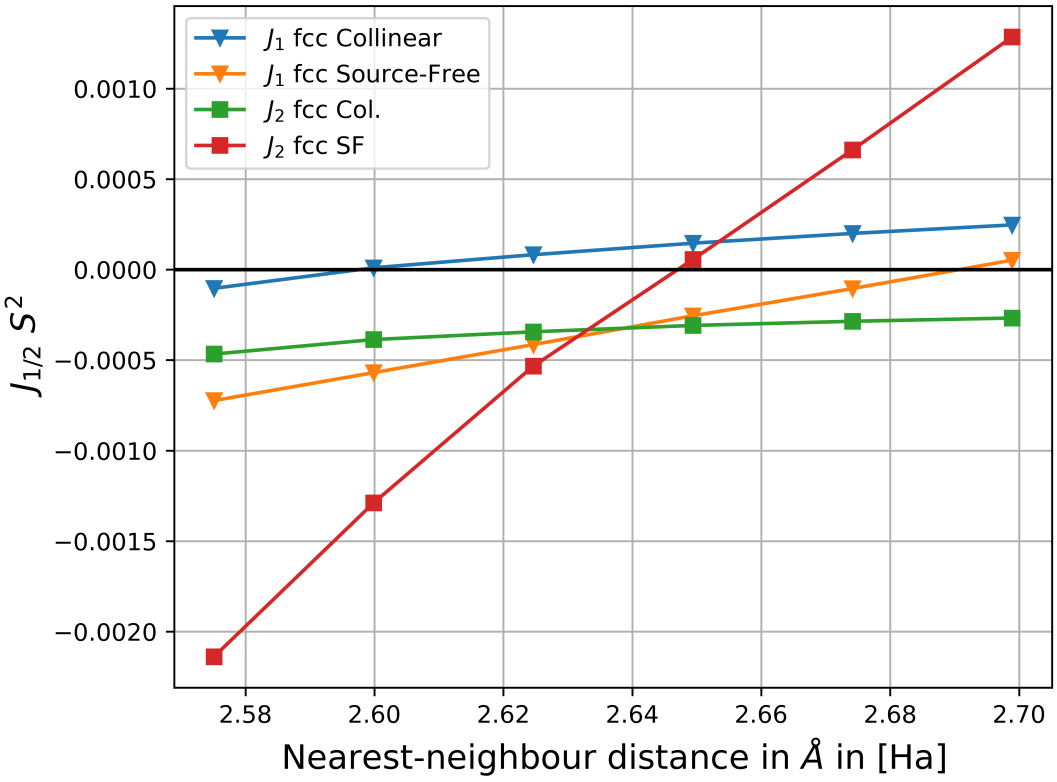

Figure 5.8.: First and second order Heisenberg coupling parameters for fcc iron structures depending on the nearest-neighbour distance.

The impact of the source-free modification is even more pronounced here. The picture is not as clear cut as in the previous case, but it can be seen that the preference of ferromagnetic states is only given for big lattice expansions, while antiferromagnetism becomes possible at a lower distance between the atoms (for comparison: 2.39 Å is the nearest-neighbour distance corresponding to the optimized fcc lattice constant that formed a non-magnetic state). It is notable, that J_2 is affected much more than J_1 between the collinear and source-free case, being several times bigger than the other couplings and therefore heavily influencing the order that the system will assume. This is similar to bcc iron, where J_2 changes sign and grows drastically to favor ferromagnetism. Only here this does not happen for the lower lattice constants, where antiferromagnetism is encouraged instead. The heavily modified couplings quantify the observation made in previous chapters, that the removal of source terms drastically alters the coupling behaviour of the iron crystal, regardless of its structure.

5.3. Discussion

Through the investigation of different ferro- and antiferromagnetic crystals, the preferred magnetic ordering and coupling behaviour of iron was compared between collinear and source-free DFT calculations. This gave deeper insight to the finding from chapter 3.3, that the moments of antiferromagnetic iron are reduced more strongly than those of the ferromagnet and can even lead to a non-magnetic state. This was verified for a range of lattice constants and therefore distances between the iron atoms in a bcc and fcc lattice. This can be used to explain how the source-free modification improves the magnetic moments. For all materials studied in [2], the magnetic moment per iron atom was significantly too large in the unmodified calculations. Additionally, all the materials under study form similar structures (between the two classes of cmme and fmmm pnictides) and show basically the same antiferromagnetic order in the iron atoms. Combining this fact with the observation of reduced antiferromagnetic moments in the iron calculations in this thesis leads to the conclusion, that the improvement is a direct consequence of this reduction. This does not support the statement from the original paper about the presence of unphysical magnetic monopoles in the pnictide materials that need to be removed, but also does not explicitly disagree with it. To better test the validity of this assumption, the divergence of the magnetic fields for converged pnictide calculations would need to be calculated and compared to simpler materials, where none should be found. It is not out of the question, that such divergences could be linked to the antiferromagnetic order with several iron atoms.

6. Conclusions and Outlook

In this thesis, the manual removal of magnetic source-fields from the exchange-correlation magnetic field as proposed in [2] and used in the Elk code was implemented into the Fleur code and tested with regard to several key properties. Likewise, the additional scaling of the input magnetization density was applied and an optimal scaling parameter was proposed based on the reproduction of the magnetic moments in elemental bulk ferromagnets. The scaling that resulted was comparable to that found in the original publication. From this point, the effect on two classes of pnictides was studied to draw comparison to the Elk code. The results were similar up to a margin of error justified by the different parametrization of the LDA functional and the different scaling. As it was noted that the magnetic moments in the Elk calculations were not aligned along the same direction experimentalists found for several of the materials, a separate calculation was carried out for one of the materials to try to improve the results this way. This was without large success, justifying the source-free modification and validating its importance. In chapter 5, however, it was highlighted, that this improvement was explicitly due to the reduction of antiferromagnetic moments and the impact of the modification on the couplings between magnetic atoms. The paper required, that the reduction was due to the removal of source terms that are unphysical and therefore warranted removal. This assumption is not backed by this thesis. To really prove this point, one would need to do calculations with an actual CDFT code, whose fields are source-free by construction. Furthermore, it was observed that the stability of source-free calculations depends greatly on the accuracy of the derivatives within the scf loop. Especially PBE-GGA calculations were only possible for the simple case of bcc iron and converged badly even then[7].
The validity of the source-free modification could be tested further by investigating other classes of materials, whose calculations by common non-collinear DFT also yield bad results for the magnetic structure, but with too low instead of too big magnetic moments. If an improvement for such a group could be produced, the notion of the

[7]Though this might be greatly improved to a recent fix, as teased in the previous footnotes.

necessity to remove the source terms would be much more acceptable. As mentioned before, a thorough investigation of the magnetic field's divergence in pnictides as compared to simple materials would also be of interest. Another quantity to investigate in this context would be the ground-state current density, that is not a variational quantity in the context of SDFT, but could easily be calculated from the ground-state wave function. From a computational point of view, the implementation could be improved by smoothing the calculated derivatives and thereby reducing the numerical noise that complicates convergence. Calculations could also be made a lot faster by implementing derivative routines and a Poisson equation solver that don't take the symmetrized basis into account. As for this thesis, all calculations needed to be done with neglected symmetry, as the intermediary quantaties needed for the modification do not adhere to the same ones as the charge and magnetization densities.

Bibliography

[1] *The Fleur Code*, www.flapw.de/, The implemented feature is only found in the development branch of the source code and does not have any documentation as of yet.

[2] S. Sharma, E. K. U. Gross, A. Sanna, and J. K. Dewhurst, "Source-free exchange-correlation magnetic fields in density functional theory," *Journal of Chemical Theory and Computation*, vol. 14, no. 3, pp. 1247–1253, Mar. 2018, ISSN: 1549-9618. DOI: 10.1021/acs.jctc.7b01049. [Online]. Available: https://doi.org/10.1021/acs.jctc.7b01049.

[3] *The Elk Code*, http://elk.sourceforge.net/.

[4] P. Hohenberg and W. Kohn, "Inhomogeneous electron gas," *Phys. Rev.*, vol. 136, B864–B871, 3B Nov. 1964. DOI: 10.1103/PhysRev.136.B864. [Online]. Available: https://link.aps.org/doi/10.1103/PhysRev.136.B864.

[5] W. Kohn and L. J. Sham, "Self-consistent equations including exchange and correlation effects," *Phys. Rev.*, vol. 140, A1133–A1138, 4A Nov. 1965. DOI: 10.1103/PhysRev.140.A1133. [Online]. Available: https://link.aps.org/doi/10.1103/PhysRev.140.A1133.

[6] U. von Barth and L. Hedin, "A local exchange-correlation potential for the spin polarized case," *J. Phys. C: Solid State Phys.*, vol. 5, no. 13, pp. 1629–1642, 1972. [Online]. Available: https://iopscience.iop.org/article/10.1088/0022-3719/5/13/012/pdf.

[7] P. Kurz, F. Förster, L. Nordström, G. Bihlmayer, and S. Blügel, "Ab initio treatment of noncollinear magnets with the full-potential linearized augmented plane wave method," *Phys. Rev. B*, vol. 69, p. 024 415, 2 Jan. 2004. DOI: 10.1103/PhysRevB.69.024415. [Online]. Available: https://link.aps.org/doi/10.1103/PhysRevB.69.024415.

[8] P. Kurz, F. Förster, L. Nordström, G. Bihlmayer, and S. Blügel, "Ab initio treatment of noncollinear magnets with the full-potential linearized augmented plane wave method," *Phys. Rev. B*, vol. 69, p. 024 415, 2 Jan. 2004. DOI: 10.1103/PhysRevB.69.024415.

[9] J. Hubbard and B. H. Flowers, "Electron correlations in narrow energy bands," *Proceedings of the Royal Society of London. Series A. Mathematical and Physical Sciences*, vol. 276, no. 1365, pp. 238–257, 1963. DOI: 10.1098/rspa.1963.0204. eprint: https://royalsocietypublishing.org/doi/pdf/10.1098/rspa.1963.0204. [Online]. Available: https://royalsocietypublishing.org/doi/abs/10.1098/rspa.1963.0204.

[10] H. Takahashi, H. Soeda, M. Nukii, *et al.*, "Superconductivity at 52k in hydrogen-substituted LaFeAsO[1-x]H[x] under high pressure," *Scientific Reports*, vol. 5, no. 1, p. 7829, Jan. 2015, ISSN: 2045-2322. DOI: 10.1038/srep07829. [Online]. Available: https://doi.org/10.1038/srep07829.

[11] Y. Kamihara, T. Watanabe, M. Hirano, and H. Hosono, "Iron-based layered superconductor LaO[1-x]F[x]FeAs (x = 0.05-0.12) with tc = 26 k," *Journal of the American Chemical Society*, vol. 130, no. 11, pp. 3296–3297, Mar. 2008, ISSN: 0002-7863. DOI: 10.1021/ja800073m. [Online]. Available: https://doi.org/10.1021/ja800073m.

[12] R. S. Kumar, J. J. Hamlin, M. B. Maple, *et al.*, "Pressure-induced superconductivity in LaFeAsO: The role of anionic height and magnetic ordering," *Applied Physics Letters*, vol. 105, no. 25, p. 251 902, 2014. DOI: 10.1063/1.4904954. eprint: https://doi.org/10.1063/1.4904954. [Online]. Available: https://doi.org/10.1063/1.4904954.

[13] N. W. Ashcroft and N. D. Mermin, *Solid State Physics*. 1976.

[14] D. J. Singh and L. Nordstrom, *Planewaves, Pseudopotentials, and the LAPW Method*. 1994.

[15] R. O. Jones and O. Gunnarsson, "The density functional formalism, its applications and prospects," *Rev. Mod. Phys.*, vol. 61, pp. 689–746, 3 Jul. 1989. DOI: 10.1103/RevModPhys.61.689. [Online]. Available: https://link.aps.org/doi/10.1103/RevModPhys.61.689.

[16] R. M. Dreizler and E. K. U. Gross, *Density Functional Theory: An Approach to the Quantum Many-Body Problem*. 1990.

[17] J. Kübler, K. .-. Höck, J. Sticht, and A. R. Williams, "Density functional theory of non-collinear magnetism," *Journal of Physics F: Metal Physics*, vol. 18, no. 3, pp. 469–483, Mar. 1988. DOI: 10.1088/0305-4608/18/3/018. [Online]. Available: https://iopscience.iop.org/article/10.1088/0305-4608/18/3/018.

[18] T. Asada and K. Terakura, "Cohesive properties of iron obtained by use of the generalized gradient approximation," *Phys. Rev. B*, vol. 46, pp. 13 599–13 602, 20 Nov. 1992. DOI: 10.1103/PhysRevB.46.13599. [Online]. Available: https://link.aps.org/doi/10.1103/PhysRevB.46.13599.

[19] P. Kurz, "Non-collinear magnetism at surfaces and in ultrathin films," Ph.D. dissertation, RWTH Aachen University, 2000.

[20] K. Capelle and E. K. U. Gross, "Spin-density functionals from current-density functional theory and vice versa:a road towards new approximations," *Phys. Rev. Lett.*, vol. 78, pp. 1872–1875, 10 Mar. 1997. DOI: 10.1103/PhysRevLett.78.1872. [Online]. Available: https://link.aps.org/doi/10.1103/PhysRevLett.78.1872.

[21] G. Vignale and M. Rasolt, "Density-functional theory in strong magnetic fields," *Phys. Rev. Lett.*, vol. 59, pp. 2360–2363, 20 Nov. 1987. DOI: 10.1103/PhysRevLett.59.2360. [Online]. Available: https://link.aps.org/doi/10.1103/PhysRevLett.59.2360.

[22] S. Blügel and G. Bihlmayer, "Full-potential linearized augmented planewave method," *NIC Series*, vol. Volume 31, 2006.

[23] D. Singh, "Ground-state properties of lanthanum: Treatment of extended-core states," *Phys. Rev. B*, vol. 43, pp. 6388–6392, 8 Mar. 1991. DOI: 10.1103/PhysRevB.43.6388. [Online]. Available: https://link.aps.org/doi/10.1103/PhysRevB.43.6388.

[24] J. C. Slater, "Wave functions in a periodic potential," *Phys. Rev.*, vol. 51, pp. 846–851, 1937. [Online]. Available: https://journals.aps.org/pr/pdf/10.1103/PhysRev.51.846.

[25] T. Loucks, *Augmented Plane Wave Method: A Guide to Performing Electronic Structure Calculations*. 1967.

[26] O. K. Andersen, "Linear methods in band theory," *Phys. Rev. B*, vol. 12, pp. 3060–3083, 8 Oct. 1975. DOI: 10.1103/PhysRevB.12.3060. [Online]. Available: https://link.aps.org/doi/10.1103/PhysRevB.12.3060.

[27] G. Michalicek, M. Betzinger, C. Friedrich, and S. Blügel, "Elimination of the linearization error and improved basis-set convergence within the flapw method," *Computer Physics Communications*, vol. 184, no. 12, pp. 2670–2679, 2013, ISSN: 0010-4655. DOI: https://doi.org/10.1016/j.cpc.2013.07.002. [Online]. Available: http://www.sciencedirect.com/science/article/pii/S0010465513002300.

[28] D. D. Koelling, "Alternative augmented-plane-wave technique: Theory and application to copper," *Physical Review B*, vol. 2, no. 2, pp. 290–298, 1972. [Online]. Available: https://journals.aps.org/prb/pdf/10.1103/PhysRevB.2.290.

[29] E. W. M. Weinert and A. J. Freeman, "Total-energy all-electron density functional method for bulk solids and surfaces," *Phys. Rev. B*, vol. 26, no. 8, pp. 4571–4578, 1982. [Online]. Available: https://journals.aps.org/prb/pdf/10.1103/PhysRevB.26.4571.

[30] D. R. Hamann, "Semiconductor charge densities with hard-core and soft-core pseudopotentials," *Physical Review Letters*, vol. 42, no. 10, pp. 662–665, 1979. [Online]. Available: https://journals.aps.org/prl/pdf/10.1103/PhysRevLett.42.662.

[31] D. A. Klüppelberg, "First-principle investigation of displacive response in complex solids," The formulae in question are found on page 43-44; a small correction was done by C.-R. Gerhorst to make the transformation matrix accurate., Ph.D. dissertation, Forschungszentrum Jülich, 2015.

[32] M. Weinert, "Solution of poisson's equation: Beyond ewald-type methods," *Journal of Mathematical Physics*, vol. 22, no. 11, pp. 2433–2439, 1981. [Online]. Available: https://aip.scitation.org/doi/pdf/10.1063/1.524800.

[33] J. P. Perdew and Y. Wang, "Accurate and simple analytic representation of the electron-gas correlation energy," *Phys. Rev. B*, vol. 45, no. 23, pp. 13 244–13 249, 1992. [Online]. Available: https://journals.aps.org/prb/pdf/10.1103/PhysRevB.45.13244.

[34] K. B. J. P. Perdew and M. Ernzerhof, "Generalized gradient approximation made simple," *Phys. Rev. Lett.*, vol. 77, no. 18, pp. 3865–3868, 1996. [Online]. Available: https://journals.aps.org/prl/pdf/10.1103/PhysRevLett.77.3865.

[35] J. P. Perdew and A. Zunger, "Self-interaction correction to density-functional approximations for many-electron systems," *Phys. Rev. B*, vol. 23, no. 10, pp. 5048–5079, 1981. [Online]. Available: https://journals.aps.org/prb/pdf/10.1103/PhysRevB.23.5048.

[36] M. Acet, H. Zähres, E. F. Wassermann, and W. Pepperhoff, "High-temperature moment-volume instability and anti-invar of gamma-Fe," *Phys. Rev. B*, vol. 49, pp. 6012–6017, 9 Mar. 1994. DOI: 10.1103/PhysRevB.49.6012. [Online]. Available: https://link.aps.org/doi/10.1103/PhysRevB.49.6012.

[37] "Crc handbook of chemistry and physics: a ready-reference of chemical and physical data, 85th ed edited by david r. lide (national institute of standards and technology). crc press llc: boca raton, fl. 2004. 2712 pp. $139.99. isbn 0-8493-0485-7.," *Journal of the American Chemical Society*, vol. 127, no. 12, pp. 4542–4542, Mar. 2005, ISSN: 0002-7863. DOI: 10.1021/ja041017a. [Online]. Available: https://doi.org/10.1021/ja041017a.

[38] H. Wijn, H. Landolt, and R. Börnstein, *Magnetische Eigenschaften von Metallen* (Landolt-Börnstein : Zahlenwerte und Funktionen aus Naturwissenschaften und Technik. Gruppe 3, Kristall- und Festkörperphysik Bd. 1). Springer, 1986, ISBN: 9780387159041. [Online]. Available: https://books.google.de/books?id=Zvw5AQAAIAAJ.

[39] J. K. Dewhurst, A. Sanna, and S. Sharma, "Effect of exchange-correlation spin-torque on spin dynamics," *The European Physical Journal B*, vol. 91, no. 10, p. 218, Oct. 2018, ISSN: 1434–6036. DOI: 10.1140/epjb/e2018-90146-1. [Online]. Available: https://doi.org/10.1140/epjb/e2018-90146-1.

[40] A. S. Sefat, A. Huq, M. A. McGuire, *et al.*, "Superconductivity in LaFe[1-x]Co[x]AsO," *Phys. Rev. B*, vol. 78, p. 104 505, 10 Sep. 2008. DOI: 10.1103/PhysRevB.78.104505. [Online]. Available: https://link.aps.org/doi/10.1103/PhysRevB.78.104505.

[41] A. Kokalj, "Xcrysden—a new program for displaying crystalline structures and electron densities," *Journal of Molecular Graphics and Modelling*, vol. 17, no. 3, pp. 176–179, 1999, ISSN: 1093-3263. DOI: https://doi.org/10.1016/S1093-3263(99)00028-5. [Online]. Available: http://www.sciencedirect.com/science/article/pii/S1093326399000285.

[42] D. Johrendt, "Structure-property relationships of iron arsenide superconductors," *J. Mater. Chem.*, vol. 21, pp. 13 726–13 736, 36 2011. DOI: 10.1039/C1JM12318A. [Online]. Available: http://dx.doi.org/10.1039/C1JM12318A.

[43] N. Qureshi, Y. Drees, J. Werner, *et al.*, "Crystal and magnetic structure of the oxypnictide superconductor LaFeAsO[1-x]F[x]: A neutron-diffraction study," *Phys. Rev. B*, vol. 82, p. 184 521, 18 Nov. 2010. DOI: 10.1103/PhysRevB.82.184521. [Online]. Available: https://link.aps.org/doi/10.1103/PhysRevB.82.184521.

[44] J. Zhao, Q. Huang, C. de la Cruz, *et al.*, "Structural and magnetic phase diagram of CeFeAsO[1-x]F[x] and its relation to high-temperature superconductivity," *Nature Materials*, vol. 7, no. 12, pp. 953–959, Dec. 2008, ISSN: 1476-4660. DOI: 10.1038/nmat2315. [Online]. Available: https://doi.org/10.1038/nmat2315.

[45] Q. Zhang, W. Tian, H. Li, *et al.*, "Magnetic structures and interplay between rare-earth Ce and Fe magnetism in single-crystal CeFeAsO," *Phys. Rev. B*, vol. 88, p. 174 517, 17 Nov. 2013. DOI: 10.1103/PhysRevB.88.174517. [Online]. Available: https://link.aps.org/doi/10.1103/PhysRevB.88.174517.

[46] A. Kreyssig, M. A. Green, Y. Lee, *et al.*, "Pressure-induced volume-collapsed tetragonal phase of $CaFe_2As_2$ as seen via neutron scattering," *Phys. Rev. B*, vol. 78, p. 184 517, 18 Nov. 2008. DOI: 10.1103/PhysRevB.78.184517. [Online]. Available: https://link.aps.org/doi/10.1103/PhysRevB.78.184517.

[47] M. Tegel, M. Rotter, V. Weiß, F. M. Schappacher, R. Pöttgen, and D. Johrendt, "Structural and magnetic phase transitions in the ternary iron arsenides SrFe2as2and EuFe2as2," *Journal of Physics: Condensed Matter*, vol. 20, no. 45, p. 452 201, Oct. 2008. DOI: 10.1088/0953-8984/20/45/452201. [Online]. Available: https://iopscience.iop.org/article/10.1088/0953-8984/20/45/452201.

[48] R. Mittal, S. K. Mishra, S. L. Chaplot, *et al.*, "Ambient- and low-temperature synchrotron x-ray diffraction study of $BaFe_2As_2$ and $CaFe_2As_2$ at high pressures up to 56 GPa," *Phys. Rev. B*, vol. 83, p. 054 503, 5 Feb. 2011. DOI: 10.1103/PhysRevB.83.054503. [Online]. Available: https://link.aps.org/doi/10.1103/PhysRevB.83.054503.

[49] A. I. Goldman, D. N. Argyriou, B. Ouladdiaf, *et al.*, "Lattice and magnetic instabilities in $CaFe_2As_2$: A single-crystal neutron diffraction study," *Phys. Rev. B*, vol. 78, p. 100 506, 10 Sep. 2008. DOI: 10.1103/PhysRevB.78.100506. [Online]. Available: https://link.aps.org/doi/10.1103/PhysRevB.78.100506.

[50] J. Zhao, W. Ratcliff, J. W. Lynn, *et al.*, "Spin and lattice structures of single-crystalline $SrFe_2As_2$," *Phys. Rev. B*, vol. 78, p. 140 504, 14 Oct. 2008. DOI: 10.1103/PhysRevB.78.140504. [Online]. Available: https://link.aps.org/doi/10.1103/PhysRevB.78.140504.

[51] Q. Huang, Y. Qiu, W. Bao, *et al.*, "Neutron-diffraction measurements of magnetic order and a structural transition in the parent $BaFe_2As_2$ compound of FeAs-based high-temperature superconductors," *Phys. Rev. Lett.*, vol. 101, p. 257 003, 25 Dec. 2008. DOI: 10.1103/PhysRevLett.101.257003. [Online]. Available: https://link.aps.org/doi/10.1103/PhysRevLett.101.257003.

[52] F. Cricchio, O. Grånäs, and L. Nordström, "Low spin moment due to hidden multipole order from spin-orbital ordering in LaFeAsO," *Phys. Rev. B*, vol. 81, 14 Apr. 2010. DOI: 10.1103/PhysRevB.81.140403. [Online]. Available: https://link.aps.org/doi/10.1103/PhysRevB.81.140403.

[53] S. Sharma, S. Shallcross, J. K. Dewhurst, *et al.*, "Magnetism in CeFeAsO[1-x]F[x] and LaFeAsO[1-x]F[x] from first principles," *Phys. Rev. B*, vol. 80, p. 184 502, 18 Nov. 2009. DOI: 10.1103/PhysRevB.80.184502. [Online]. Available: https://link.aps.org/doi/10.1103/PhysRevB.80.184502.

[54] V. I. Anisimov, F. Aryasetiawan, and A. I. Lichtenstein, "First-principles calculations of the electronic structure and spectra of strongly correlated systems: The LDA+U method," *Journal of Physics: Condensed Matter*, vol. 9, no. 4, pp. 767–808, Jan. 1997. DOI: 10.1088/0953-8984/9/4/002. [Online]. Available: https://iopscience.iop.org/article/10.1088/0953-8984/9/4/002.

[55] J. D. Jackson, *Classical Electrodynamics*. 1962.

[56] D. D. Koelling and B. N. Harmon, "A technique for relativistic spin-polarised calculations," *Journal of Physics C: Solid State Physics*, vol. 10, no. 16, pp. 3107–3114, 1977. [Online]. Available: https://iopscience.iop.org/article/10.1088/0022-3719/10/16/019/pdf.

[57] J. Kübler, K.-H. Höck, J. Sticht, and A. R. Williams, "Local spin-density functional theory of noncollinear magnetism (invited)," *Journal of Applied Physics*, vol. 63, no. 8, pp. 3482–3486, 1988. DOI: 10.1063/1.340744. eprint: https://doi.org/10.1063/1.340744. [Online]. Available: https://doi.org/10.1063/1.340744.

[58] Y. Wang and J. P. Perdew, "Spin scaling of the electron-gas correlation energy in the high-density limit," *Phys. Rev. B*, vol. 43, no. 11, pp. 8911–8916, 1991. [Online]. Available: https://journals.aps.org/prb/pdf/10.1103/PhysRevB.43.8911.

[59] L. W. S. H. Vosko and M. Nusair, "Accurate spin-dependent electron liquid correlation energies for local spin density calculations: A critical analysis," *Canadian Journal of Physics*, vol. 58, no. 8, pp. 1200–1211, 1980. [Online]. Available: https://www.nrcresearchpress.com/doi/pdf/10.1139/p80-159.

[60] A. R. W. V. L. Moruzzi J. F. Janak, *Calculated Electronic Properties of Metals*. 1978.

[61] A. I. L. A. B. Shick and W. E. Pickett, "Implementation of the lda+u method using the full-potential linearized augmented plane-wave basis," *Phys. Rev. B*, vol. 60, no. 15, pp. 10 763–10 769, 1999. [Online]. Available: https://journals.aps.org/prb/pdf/10.1103/PhysRevB.60.10763.

[62] J. Kübler, "Magnetic moments of ferromagnetic and antiferromagnetic bcc and fcc iron," *Physics Letters A*, vol. 81, no. 1, pp. 81–83, 1981, ISSN: 0375-9601. DOI: https://doi.org/10.1016/0375-9601(81)90311-X. [Online]. Available: http://www.sciencedirect.com/science/article/pii/037596018190311X.

[63] R. D. R. F. C. M. R. C. S. I. H. H. G. Lamura T. Shiroka P. Bonfà S. Sanna and M. Putti, "Crossover between magnetism and superconductivity in LaFeAsO with low h-doping level," *Journal of Physics: Condensed Matter*, vol. 26, no. 29, 2014. [Online]. Available: https://iopscience.iop.org/article/10.1088/0953-8984/26/29/295701/pdf.

[64] H. Maeter, H. Luetkens, Y. G. Pashkevich, *et al.*, "Interplay of rare earth and iron magnetism in RFeAsO (R=La, Ce, Pr, and Sm): Muon-spin relaxation study and symmetry analysis," *Physical Review B*, vol. 80, no. 9, Sep. 2009, ISSN: 1550-235X. DOI: 10.1103/physrevb.80.094524. [Online]. Available: http://dx.doi.org/10.1103/PhysRevB.80.094524.

[65] F. Birch, "Finite elastic strain of cubic crystals," *Phys. Rev.*, vol. 71, pp. 809–824, 11 Jun. 1947. DOI: 10.1103/PhysRev.71.809. [Online]. Available: https://link.aps.org/doi/10.1103/PhysRev.71.809.

A. The Birch-Murnaghan equation of state

At several points in this thesis, structural relaxations were done. The curves represent the dependency of the total energy of the unit cell vs. its volume by scaling up the lattice constants within a certain range. To find the optimized lattice constant by energy minimization, the values are fitted against the Birch-Murnaghan equation of state, that relates the internal energy E to the unit cell volume V:

$$E(V) = E_0 + \frac{9V_0B_0}{16}\left\{\left[(\frac{V_0}{V})^{2/3} - 1\right]^3 B_0' + \left[(\frac{V_0}{V})^{2/3} - 1\right]^2 \left[6 - 4(\frac{V_0}{V})^{2/3}\right]\right\}$$

The resulting fitting parameters are the reference energy E_0, the bulk modulus B_0, its pressure derivative B_0' and the optimized volume V_0 from which the optimized lattice constant is calculated.

Danksagung

An erster Stelle gilt mein Dank Prof. Dr. Stefan Blügel, an den ich herangetreten bin als ich nicht weiter wusste mit meinem Masterstudium und in dessen Institut ich mich nun sehr wohl fühle. Seine Begeisterung für jedermanns Arbeit sucht ihresgleichen. Auch danke ich ihm für seine Bemühungen in Richtung der Ermöglichung einer anschließenden Doktorarbeit.
Ich danke allen Mitarbeitern des Instituts, an die ich mit meinen zahlreichen Fragen zu ihren jeweiligen Expertisen herantreten konnte und stets schnelle und präzise Antworten bekommen habe. Vor allem sind hier hervorzuheben Christian-Roman Gerhorst wegen seiner Unterstüzung im Bezug auf notwendige Ableitungsroutinen und der Motivation hin zum Thema der anschließenden Doktorarbeit, Dr. Gregor Michalicek und Dr. Gustav Bihlmayer bezüglich ihres umfassenden Wissens in komplizierten Sektionen des Codes und Dr. Daniel Wortmann, der wohl mit Abstand die meisten meiner Fragen im Bezug auf nicht-kollinearen Magnetismus ertragen und beantworten musste. Seine Geduld hat maßgeblich zum Erfolg dieser Arbeit beigetragen.
Prof. Dr. Samir Lounis danke ich für die Übernahme des Zweitgutachtens und die damit verbundene schnelle Zeitplanung und Terminfindung, trotz des erschwerenden Faktors der Corona-Pandemie.
Ich danke Ute Winkler für die kompetente Hilfe bei bürokratischen Angelegenheiten, durch die ich alleine niemals durchblicken würde.
Abseits dessen danke ich allen meinen Freunden und meiner Familie, die mich immer unterstützen und mich von der Arbeit ablenken, wenn es wirklich nicht Zeit ist zum Arbeiten. In diesem Zusammenhang gilt mein größter Dank meinem Bürokollegen Robin Hilgers, dessen zweite Meinung für konzeptionelle Probleme, Schwierigkeiten bei der Fehlerfindung und allgemeine Unterstützung für mich essentiell geworden ist. Ich blicke mit Enthusiasmus darauf, drei weitere Jahre mit ihm das Büro und das Auto zu teilen und hoffe auf weiterhin fruchtbare Zusammenarbeit.